Ocean Engineering 370 (2026) 129153

Contents lists available at ScienceDirect

Ocean Engineering

journal homepage: www.elsevier.com/locate/oceaneng

Research paper

YingLong-T: A compact triphibious vehicle prototype with a unified powertrain for multi-domain locomotion

Le Huang, Shuxiang Guo *, Qirong Lei, Miaozhang Shen, Chunying Li, Siying Pu, Shuaixin Peng, Guoheng Ma, Jinglei Nie, Pengcheng Li

Southern University of Science and Technology, Shenzhen, Guangdong, 518055, China

ARTICLE INFO

Keywords:
Triphibious vehicle
Unified powertrain
Dual-medium propeller
Cross-domain mobility

ABSTRACT

Triphibious vehicles capable of operating in air, on land, and underwater can support missions in complex environments, but existing platforms often require separate propulsion and subsystems. This paper presents YingLong-T, a compact triphibious vehicle with a integrated triangular body and a unified powertrain. The integrated body serves as the load-bearing airframe, sealed equipment enclosure, and primary buoyancy volume. Each of its three support arms carries a reconfigurable propulsion unit and a passive wheel. The shared propulsion units provide tri-rotor flight, propeller-driven ground rolling, and Y3 underwater propulsion. A single flight controller and customized firmware coordinate the three mobility domains. Positive buoyancy and propulsion reorientation enable staged air–water transitions without active buoyancy adjustment. A 2.5 kg prototype demonstrated manual flight with a 0.85 kg payload, a maximum ground speed of 6.1 m/s, a terrestrial tracking RMSE of 45.6 mm, a mean submerged speed of 1.20 m/s, and steady-state errors in yaw and depth control within ±5° and ±2 cm, respectively, in the representative records. All seven evaluated cross-domain cycles were completed under the reported pool, river, and coastal conditions. Across the three coastal trials, the mean end-to-end durations were 10.1, 5.4, and 8.0 s for LAND–AIR, AIR–WATER, and WATER–AIR, respectively. The results establish prototype feasibility under the tested conditions; broader marine operating envelopes, long-term durability, and offshore readiness remain to be established.

1. Introduction

Triphibious vehicles extend amphibious and hybrid aerial–underwater vehicles by combining aerial, terrestrial, and aquatic mobility on one platform (Wang et al., 2025; Z. Guo et al., 2019; Yang et al., 2022; Li et al., 2026). This capability is relevant to marine inspection, where such vehicles can reduce personnel exposure in hazardous or inaccessible areas (Mitchell et al., 2022). As the motivating scenario in Fig. 1 illustrates, a triphibious vehicle could approach an offshore structure by air, reposition on a deck, and then submerge to inspect its foundations without handoffs among separate vehicles. The scenario defines the intended task sequence; it is not a deployment demonstrated in this study.

Achieving that sequence on a compact vehicle creates coupled design requirements. Flight penalizes mass and volume, ground motion requires support and traction, and submerged operation requires sealing, buoyancy management, hydrodynamic performance, and underwater control authority. The transitions between these operating regimes also require coordinated reconfiguration and control. Existing triphibious platforms commonly aggregate domain-specific locomotion modules, reuse air-oriented propellers directly in water, or limit aquatic operation to the surface (Z. Guo et al., 2019; Chaikalis et al., 2023; Canelon et al., 2021; Yang et al., 2022). These choices provide multi-domain mobility but retain trade-offs in redundant mass, underwater efficiency, mechanical complexity, and controller coordination.

This paper presents YingLong-T to investigate whether those trade-offs can be managed through system-level co-design rather than by adding a complete propulsion and control subsystem for each domain. The objective is to demonstrate prototype-level integration of a streamlined buoyant body, a unified tiltable powertrain, and a single hardware/firmware control implementation for aerial flight, terrestrial rolling, underwater manoeuvring. The main contributions are as follows:

1. An integrated triangular body jointly provides the load-bearing airframe, sealed electronics enclosure, and primary buoyancy volume. Three shared propulsion units support tri-rotor flight, propeller-driven three-wheeled terrestrial rolling, and Y3 underwater propulsion.

* Corresponding author.
E-mail address: guo.shuxiang@sustech.edu.cn (S. Guo).

https://doi.org/10.1016/j.oceaneng.2026.129153
Received 15 April 2026; Received in revised form 8 October 2026; Accepted 25 October 2026
Available online 5 November 2026
0029-8018/© 2026 Elsevier Ltd. All rights are reserved, including those for text and data mining, AI training, and similar technologies.



Fig. 1. Overview of YingLong-T and a motivating offshore-platform inspection scenario. The scenario illustrates the intended multi-domain task sequence and does not represent a demonstrated operational deployment.

2. A unified tiltable powertrain reuses one motor set across all three domains. Each same-side aerial–underwater propeller assembly directly couples the underwater propeller to the motor and drives the aerial propeller through a single one-way clutch, avoiding separate ground-drive and underwater-thruster motor sets.
3. Positive buoyancy and propulsion-unit reorientation enable staged bidirectional air–water transitions without active buoyancy adjustment. Buoyancy maintains propeller clearance during water exit, whereas a reorientation-induced centre-of-gravity shift and sequential thrust application enable controlled submergence.
4. A single flight controller and customized firmware coordinate all three domains through domain-specific controller adapters, domain-dependent actuator mappings, and guarded switching logic.

The resulting 2.5 kg prototype is evaluated through propeller tests and aerial, terrestrial, underwater, and cross-domain experiments, including seven manually controlled transition cycles. These tests establish the feasibility and present evidence boundary of the integrated architecture.

2. Related work

Triphibious vehicles add terrestrial mobility to the aerial, aquatic, and transition capabilities studied in hybrid aerial–underwater vehicles (HAUVs). The review is therefore organized around the system-level decisions that motivate YingLong-T: structural integration, propulsion reuse and air–water transition, and multi-domain control. Adjacent dual-domain vehicles are included only where their design principles are transferable to a three-domain platform.

Triphibious architecture and structural integration. Dual-domain vehicles illustrate the basic integration trade-off. Adaptive limbs and repurposable appendages can reduce dedicated hardware but require additional transformation and control (Baines et al., 2022; Sihite et al., 2023); systems that combine wheels or legs with separate propulsors retain stronger domain specialization but share less of the actuation (Xing et al., 2022; Cao et al., 2023). A triphibious vehicle must manage this trade-off while also satisfying low airborne mass, sealing, buoyancy, ground support, and low submerged drag.

Reported triphibious systems broadly follow three architectural routes. The first aggregates domain-specific subsystems, as in the mother–child tri-habitat concept (J. Guo et al., 2019) and hybrid ground–air–water vehicles (Chaikalis et al., 2023; Evangeliou et al., 2023). The platform of Chaikalis et al. (2023), for example, combines a coaxial tricopter, omnidirectional wheels, aquatic propulsors, and added flotation. This preserves domain-specific actuation but increases the hardware, sealing interfaces, and coordination required, and its reported aquatic operation is confined to the water surface.

The second route reuses propulsion across domains. The all-environment vehicle of Z. Guo et al. (2019) employs a coaxial multirotor system in air, on land, and in water. Zhong et al. (2021) and TriphiBot (Li et al., 2026) use rotor thrust with passive wheels for terrestrial and aquatic motion, whereas Omnibot (Canelon et al., 2021) shares screw drives between land and water but retains a separate quadrotor propulsion set. Directly reusing air-oriented rotors reduces actuator count but compromises underwater efficiency; partial reuse retains duplicated mechanisms. Some reconfigurable designs also remain simulation-based (Yu and Chen, 2019; Zhong et al., 2021), limiting evidence of vehicle-level performance across all three media.

The third route uses the body itself as part of the locomotion mechanism. The cylindrical platform of Yang et al. (2022) rolls on land and reorients three ducted propulsors for flight and surface-water motion. This produces a compact configuration, but does not provide submerged locomotion and requires the water surface as an intermediate state for LAND-AIR transition. Together, these routes leave a coupled design problem: integrating the airframe, sealed enclosure, buoyancy, and ground support without sacrificing controlled submerged operation or adding a complete propulsion subsystem for each domain.

Air–water propulsion and transition. HAUVs provide the closest basis for propulsion and transition across the air–water interface (Liu et al., 2026). Dedicated systems, such as Nezha-IV's aerial propellers and underwater thrusters (Jin et al., 2023), allow each propulsor to be designed for its medium (Sun et al., 2023; Bi et al., 2024; Gao et al., 2023), but add actuators, mass, volume, and sealing interfaces. At the other extreme, operating air-oriented propellers directly underwater minimizes hardware (Alzu'bi et al., 2015; Qin et al., 2023; Wang et al., 2024), but constrains rotational speed and aquatic efficiency. Passive folding can reduce underwater drag (Li et al., 2022), although it does not remove the cross-medium propeller-design compromise.

Table 1
Contextual comparison of representative triphibious platforms.

Parameter	AEM[c]	TR-TRS[d]	NTR[e]	GAWHV[f]	Omnibot[g]	TriphiBot[h]	YingLong-T (Ours)
Size (mm)	–	550 × 500×–	ϕ 410 × 120[b]	1148 × 1108 × 600	–	350 × 340 × 340	514 × 554 × 280
Mass (kg)	2.2	~4.0	3.88	7.5	1.61	1.1	2.5
Primary propulsion	Shared	Partially shared	Shared	Separate	Separate	Shared	Shared
Reported aquatic capability	Submerged (low efficiency)	Submerged (simulation)	Surface only	Surface only	Submerged (limited)	Submerged (low efficiency)	Submerged yaw and depth
Ground speed (m/s)	–	–	–	0.5	–	3.0	6.1
Transition duration (s)	–	–	–	–	–	1.5	5.4 (A–W); 8.0 (W–A)
Validation	Prototype[a]	Simulation	Prototype[a]	Prototype[a]	Prototype[a]	Prototype	Prototype

Shared indicates that the same primary propulsion motors are reused across the reported domains; *partially shared* indicates partial cross-domain reuse; and *separate* indicates domain-specific propulsion actuator sets. This classification does not imply complete actuator commonality. "–" indicates data not reported. Transition-duration definitions are source-specific; for YingLong-T, A–W and W–A denote the mean end-to-end AIR–WATER and WATER–AIR durations, respectively.

[a] A physical prototype was demonstrated, but key quantitative metrics were not reported.

[b] The source separately reports a 100 mm deformation height in addition to the 120 mm body height.

[c] Z. Guo et al. (2019).

[d] Zhong et al. (2021).

[e] Yang et al. (2022).

[f] Chaikalis et al. (2023) and Evangeliou et al. (2023).

[g] Canelon et al. (2021).

[h] Li et al. (2026).

A third strategy adapts a shared motor to the active medium. TJ-FlyingFish (Liu et al., 2023) reverses its motors to select the ratio of a dual-speed transmission and tilts the propulsion units for underwater thrust vectoring. Dipper (Rockenbauer et al., 2021) selects specialized aerial and underwater propellers using two oppositely oriented one-way clutches and a shaft to the rear underwater propeller. Nezha-SeaDart III (Jin et al., 2026) likewise switches medium-specific propellers by motor reversal in a more compact tail-sitter installation. These mechanisms improve medium-specific propulsion, but gear trains, paired clutches, or extended transmission paths add losses, components, and packaging demands. For a compact triphibious vehicle, the unresolved requirement is a lower-component-count selector that can also tilt for ground propulsion and underwater thrust allocation.

Transition design is coupled to propulsion selection, buoyancy, and vehicle attitude. Dipper uses a morphing fixed-wing configuration for dynamic entry and exit (Rockenbauer et al., 2021); Nezha-IV uses dedicated propulsion for repeated ocean transitions (Jin et al., 2023); and the vehicle of Qin et al. (2023) combines positive buoyancy with tilting motors for diving and water exit. These studies establish that buoyancy and propulsion reorientation can assist the transition sequence. They do not, however, address how the same mechanisms should be integrated with terrestrial support and a shared three-domain powertrain.

Multi-domain control integration. Mechanical reuse across distinct regimes requires domain-specific feedback, actuator remapping, guarded switching, and one unambiguous command source. HAUVs use medium-dependent controllers with thrust allocation, tilting propulsion, or transition logic (Bai et al., 2023; Liu et al., 2023; Wang et al., 2024). A triphibious platform additionally requires ground propulsion and steering while its actuators change function between domains.

Existing implementations span subsystem coordination and integrated control. Chaikalis et al. (2023) use separate autopilot stacks under a supervisory computer, whereas Omnibot (Canelon et al., 2021) separates multirotor flight from screw-drive control. TriphiBot (Li et al., 2026) more recently reports unified HNMPC–PID control with field-oriented motor drives. These studies establish supervisory or algorithmic integration, but do not show whether domain-specific control and actuator mappings for the medium-specific propellers and tilting units used here can run on one flight controller and one firmware without autopilot handoff.

Summary of research gaps. The literature thus highlights a mission-dependent trade-off. Domain-specific subsystems can improve efficiency and control authority within each domain, but add airborne mass, volume, sealing interfaces, and coordination complexity. Reusing propulsion hardware across domains reduces duplication, but may compromise efficiency in individual domains, redundancy, or mechanical simplicity. Research on HAUVs informs air–water propulsion and transitions, while triphibious platforms must additionally accommodate ground locomotion.

Table 1 therefore compares representative triphibious systems with separate, partially shared, and shared primary propulsion. The dimensions describe system integration and demonstrated scope rather than establish a performance ranking: platforms differ in scale, mission, configuration, test environment, and metric definitions. Values for prior systems are taken from the cited original publications; YingLong-T values are from the experiments reported here.

As Table 1 shows, existing systems differ substantially in propulsion sharing, aquatic scope, and validation. The combined gap relevant to this study is a compact prototype that (i) integrates the airframe, sealed enclosure, and buoyancy volume; (ii) reuses one motor set with medium-specific propellers across all three domains; (iii) uses the same tilting units and positive buoyancy for staged air–water transitions; and (iv) coordinates the resulting actuator remapping on one controller running a single firmware.

Accordingly, this study investigates whether a compact vehicle with an integrated buoyant body, a shared reconfigurable powertrain, and a single flight controller can support aerial flight, ground rolling, underwater propulsion, and bidirectional AIR–LAND and AIR–WATER transitions. It also examines the trade-offs that this integration introduces in efficiency, redundancy, complexity, and reliability.

The remainder of this paper is organized as follows. Section 3 presents the mechanical design and integrated body–propulsion architecture. Section 4 describes the single-firmware multi-domain control implementation. Section 5 details the domain-specific actuator configurations and guarded cross-domain transition strategy. Section 6 reports the experimental validation. Finally, Section 7 concludes the paper and outlines future work.

3. Platform design

3.1. Overall architecture

YingLong-T was designed for sequential inspection tasks that require aerial flight, short-range travel on flat surfaces, forward-dominant submerged motion, and bidirectional air–water transitions. Rough-terrain mobility, fully actuated six-degree-of-freedom underwater station keeping, and fault tolerance after propulsion-unit failure are beyond the scope of the present prototype.

YingLong-T is built around an integrated triangular body. The integrated body serves as the load-bearing airframe, sealed equipment enclosure, and primary buoyancy volume. Each of its three support arms carries a reconfigurable propulsion unit and a passive wheel (Fig. 2). Throughout, *front* and *aft* denote fixed mounting positions relative to the AIR/LAND body-forward direction; forward travel in WATER is opposite (Fig. 6). The three propulsion units, mounted in a two-front/one-aft triangular arrangement, serve all three domains. In AIR, the three propulsion units form a tri-rotor. In LAND, two fixed front wheels and a steerable rear caster form a three-point support polygon; the front propellers propel the vehicle while its passive wheels roll and the aft motor is disabled. In WATER, the two laterally separated front units are oriented horizontally to generate forward thrust and a differential-thrust yaw moment, while the vertically oriented aft unit supplies thrust for depth regulation. This reuse eliminates dedicated wheel-drive motors and a separate underwater-thruster set; steering and braking actuators remain specific to LAND. The domain-dependent configurations are detailed in Section 5.1.

The body is 3D-printed from PA6-CF and coated externally with epoxy to limit moisture ingress and salt-spray exposure, as the material has a saturated water absorption of 2.35%. An end cap fitted with FKM O-rings and silicone grease seals the hull opening, while the depth sensor and GPS module are mounted externally. The vehicle measures $514 \times 554 \times 280\,\text{mm}$ ($L \times W \times H$) with the propellers deployed and $260 \times 300 \times 280\,\text{mm}$ with them folded, with a total mass of 2.5 kg including the battery.

Section 3.2 details the body-shape rationale and hull-design trade-offs, while Section 3.3 compares rotor layouts at a fixed footprint.

3.2. Hull-design workflow and buoyancy–mass–stiffness trade-off

The hull serves as a watertight enclosure, load-bearing airframe, and primary buoyancy volume. Its design must balance footprint constraints, equipment space requirements, structural stiffness, hydrodynamic drag, mass, and positive buoyancy.

Fused deposition modelling (FDM) was selected for low-cost iteration and fabrication of the integrated hull without dedicated moulds. Material selection considered density, stiffness under propulsion loads, impact resistance during landing, and heat resistance above 100 °C to accommodate potential local ESC heating. Manufacturer data give a density of $1.09\,\text{g/cm}^3$ and a dry XY flexural modulus of 5460 MPa for PA6-CF (Bambu Lab, a), compared with $1.20\,\text{g/cm}^3$ and 2310 MPa for PC (Bambu Lab, b), and $1.14\,\text{g/cm}^3$ and 3670 MPa for PA6-GF (Bambu Lab, c). PA6-CF also has a reported heat-deflection temperature of 186 °C at 0.45 MPa. PA6-CF was therefore selected for its combination of low density, high stiffness, and heat resistance. The epoxy coating described in Section 3.1 addresses the material's moisture sensitivity.

The shell structure was designed to balance stiffness and mass through the choice of wall thickness and printing parameters. Wall thickness and continuous walls contribute to bending and attachment stiffness, while partial infill limits material use and printing time. At a fixed outer geometry, thicker walls increase mass and reduce internal volume and net buoyancy, whereas thinner walls reduce local rigidity. The final wall thickness and printing parameters were selected based on findings from previous studies (Gómez-Ortega et al., 2024; Gonzalez et al., 2023), together with our preliminary fabrication trials and prototype testing. These comprised a nominal 2 mm wall thickness, a 0.4 mm nozzle, a 0.2 mm layer height, a wall-loop count of six, and 30% three-dimensional honeycomb infill in regions with an infill core.

The overall layout follows the triangular arrangement shared by the tri-rotor, three-wheel, and Y3 configurations. Propulsion-unit spacing and maximum propeller diameter constrain the footprint (Section 3.3); equipment dimensions and installation clearances determine the required internal volume V_{req}. The tapered triangular contour drew visual inspiration from the manta ray. Candidate contours were evaluated within the footprint under the same CFD conditions, and the contour with the lowest simulated total underwater resistance among those candidates was retained as Γ^*.

With the material, printing parameters, and planform fixed, height H controls the remaining mass–volume trade-off. The CAD sizing process can be expressed as

$$\begin{aligned} \underset{H}{\text{minimize}} \quad & m_{\text{tot}}(H) = m_{\text{fix}} + \rho_{\text{s}} V_{\text{print}}(H) \\ \text{subject to} \quad & V_{\text{int}}(H) \geq V_{\text{req}}, \\ & \Delta B_{\min} \leq \rho_{\text{w}} g V_{\text{disp}}(H) - m_{\text{tot}}(H) g \leq \Delta B_{\max}. \end{aligned} \tag{1}$$

Here, m_{fix} is the total mass of all components other than the shell, including the electrical control system and battery inside the hull, and externally mounted sensors, motors, servos, propellers, wheels, and other components. This mass is held constant during height selection. $V_{\text{print}}(H)$ is the deposited PA6-CF volume accounting for the wall and infill settings; $V_{\text{int}}(H)$ is the usable internal volume; and $V_{\text{disp}}(H)$ is the total displaced volume of the fully submerged vehicle. The densities of PA6-CF and water are ρ_{s} and ρ_{w}. For the fixed component layout, the lower bound $\Delta B_{\min} > 0$ is set by the requirements for passive surfacing and sufficient clearance for all three integrated propellers above the water surface at static floating equilibrium, with all three propulsion units set to their vertical AIR orientation. The upper bound $\Delta B_{\max}$ is set so that, in the floating WATER configuration with the two front propulsion units oriented horizontally, both underwater propellers are fully submerged and reverse propulsion can drive the vehicle below the surface.

Increasing height provides equipment and displacement volume but adds printed mass, so the objective favours a compact hull that meets both packaging and positive-buoyancy requirements. The buoyancy bounds and hull height were initially determined from CAD mass and volume calculations and subsequently adjusted based on prototype tests. The resulting design has a hull height of 58 mm, a shell mass of 189 g (approximately 7.6% of the 2.5 kg vehicle mass), and approximately 10 N of net positive buoyancy.

3.3. Footprint-constrained comparison of tri-rotor and quad-rotor layouts

For an N-rotor vehicle with circumscribed diameter D, the maximum propeller diameter is (Quan, 2017)

$$d_{p,N}(D) = \frac{D \sin(\pi/N) - \delta}{1 + \sin(\pi/N)}, \tag{2}$$

where N is the number of rotors, D is the circumscribed vehicle diameter, δ is the required tip-clearance margin, and $d_{p,N}(D)$ is the maximum allowable propeller diameter. Because motors and propellers are available only in discrete sizes, each candidate s represents a matched propeller–motor–ESC combination. It is characterized by its propeller diameter $d_{p,s}$, input-power curve $P_s(T)$, maximum thrust $T_{\max,s}$, and current and torque limits $I_{\max,s}$ and $Q_{\max,s}$. For a given D, the feasible set is $S_N(D) = \{s \mid d_{p,s} \leq d_{p,N}(D)\}$, and the optimal candidate is selected by

$$s_N^*(D) = \arg\min_{s \in S_N(D)} N P_s\left(\frac{Mg}{N}\right), \tag{3}$$

subject to

$$T_{\max,s} \geq \frac{\lambda M g}{N}, \qquad I_s \leq I_{\max,s}, \qquad Q_s \leq Q_{\max,s}, \tag{4}$$

Here, $s_N^*(D)$ is the selected combination, M is the take-off mass, g is gravitational acceleration, and Mg/N is the required hover thrust per rotor. The function $P_s(T)$ gives the input power of candidate s at thrust T, while I_s and Q_s are its current and motor torque at the checked operating point. The coefficient λ is the required thrust-to-weight ratio and was set to 2. The performance curves and limits were taken from manufacturer static tests or datasheets.

The two selection metrics were hover efficiency and theoretical payload allowance. The compared layouts are denoted by $N_1 = 3$

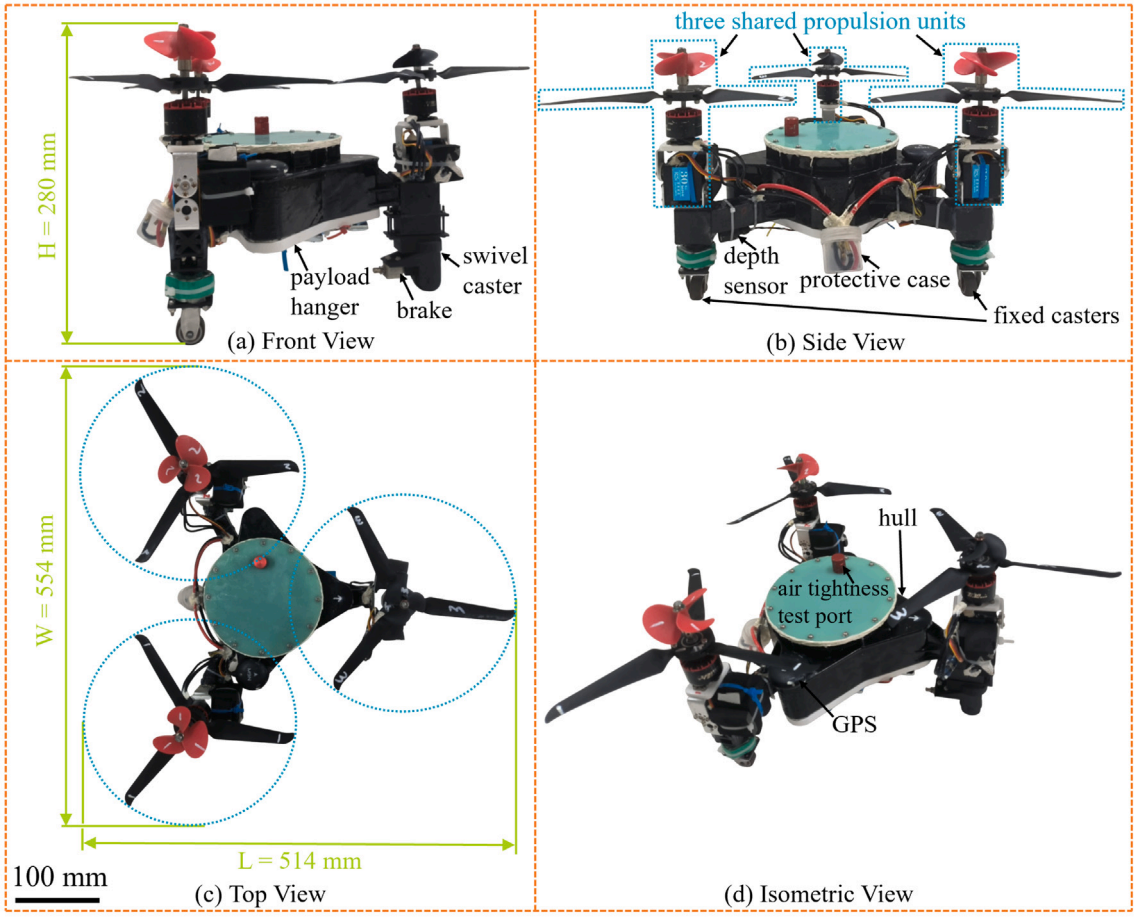


Fig. 2. YingLong-T prototype: (a) front, (b) side, (c) top, and (d) isometric views, with principal components and deployed dimensions indicated. The triangular body combines the load-bearing airframe, sealed equipment enclosure, and primary buoyancy volume. The payload hanger provides multiple attachment points for external payloads. Each arm carries a reconfigurable propulsion unit and a passive wheel, enabling the same three propulsion units to serve AIR, LAND, and WATER without dedicated wheel-drive motors or a separate underwater-thruster set.

and $N_2 = 4$. At the same take-off mass, hover efficiency is inversely proportional to input power; therefore, the efficiency ratio is

$$R_\eta(D) = \frac{P_{h,N_2}(D)}{P_{h,N_1}(D)}, \qquad P_{h,N}(D) = N P_{s_N^*}\left(\frac{Mg}{N}\right). \tag{5}$$

where $P_{h,N}(D)$ is the total hover power of the selected N-rotor system. Thus, $R_\eta > 1$ indicates that the tri-rotor requires less hover power than the quad-rotor.

The corresponding payload ratio is

$$R_{\text{pay}}(D) = \frac{m_{\text{pay},N_1}(D)}{m_{\text{pay},N_2}(D)}, \qquad m_{\text{pay},N} = \frac{N T_{\max,s_N^*}}{\lambda g} - m_c - m_{\text{sys},N}, \tag{6}$$

where $m_{\text{pay},N}$ is the theoretical payload allowance, m_c is the common non-propulsion mass, and $m_{\text{sys},N}$ is the propulsion installation mass. Specifically, $m_{\text{sys},N} = N(m_{\text{motor}} + m_{\text{prop}} + m_{\text{ESC}} + m_a)$, where m_{motor}, m_{prop}, and m_{ESC} are the component masses of the selected combination and m_a is the mass of the arm, wiring, mounting interface, and local structure associated with each propulsion unit. In Eq. (6), $T_{\max,s_N^*}$ is the maximum thrust of the selected combination and is expressed as a force.

For the present prototype, the deployed aerial footprint was constrained to a circumscribed diameter of $D = 600$ mm to preserve platform compactness, while a minimum tip-clearance margin of $\delta = 20$ mm was imposed to prevent interference between adjacent propellers. Under these design constraints, Eq. (2) gives maximum allowable propeller diameters of 267.7 mm (10.54 in) and 236.8 mm (9.32 in) for the tri-rotor and quad-rotor layouts, respectively. Because commercial aerial propellers are specified by nominal inch sizes, we selected diameters of 10.5 in (266.7 mm) and 9 in (228.6 mm), respectively. T-MOTOR and HQProp candidates were screened using their published static-thrust data (T-MOTOR, 2026), with the same SkyWalker V2 6S bidirectional ESC specified for both layouts. Table 2 lists the best candidates within this database.

The selected tri-rotor and quad-rotor propulsion systems provide total maximum static thrusts of 14.205 kgf and 11.691 kgf, respectively. Thus, the tri-rotor provides 21.5% greater maximum thrust. To isolate propulsion efficiency from differences in installation mass, the two layouts were evaluated at a common gross mass of 3.35 kg, equal to the tested take-off mass of YingLong-T (2.5 kg vehicle mass plus a 0.85 kg payload). The required hover thrusts are therefore 1.1167 kgf per rotor for the tri-rotor and 0.8375 kgf per rotor for the quad-rotor. Interpolation of the published manufacturer data at these operating points gives total hover powers of 607.3 and 680.7 W, respectively. At this common-mass design point, the selected tri-rotor requires 10.8% less hover power, corresponding to a 12.1% higher thrust-to-power efficiency.

Assuming $m_a = 50$ g, the estimated propulsion installation masses are 757.8 g and 827.2 g for the tri-rotor and quad-rotor layouts, respectively, with the tri-rotor layout giving an 8.4% reduction relative to the quad-rotor layout. With the same non-propulsion mass of $m_c = 1800$ g, Eq. (6) yields theoretical payload allowances of 4.54 kg for the tri-rotor and 3.22 kg for the quad-rotor, based on the available thrust margin. The ratio $R_{\text{pay}}(600) = 1.412$ indicates that the tri-rotor's theoretical payload allowance is 41.2% greater than that of the quad-rotor.

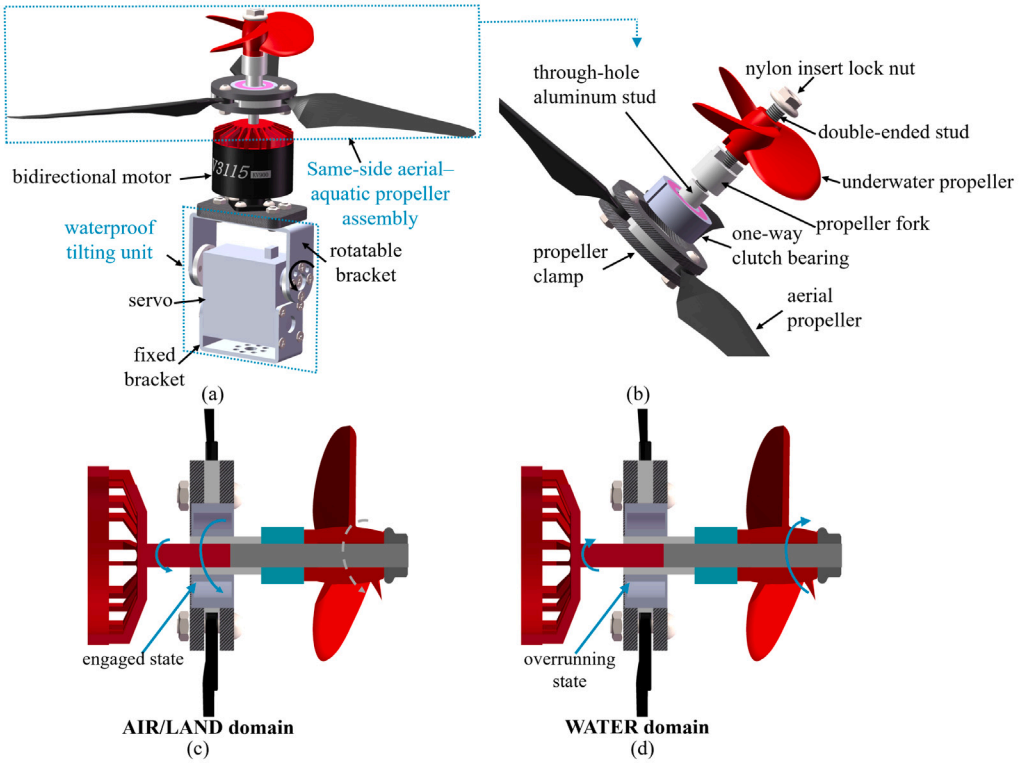


Fig. 3. Unified powertrain and propulsion unit: (a) tilting mount, motor, and same-side aerial–underwater propeller assembly; (b) exploded view showing direct drive of the underwater propeller and a single one-way clutch coupling the aerial propeller; (c) AIR/LAND operation, in which the engaged clutch drives the aerial propeller and the directly fixed underwater propeller co-rotates in the same direction; and (d) forward WATER operation, in which the clutch overruns, the motor directly drives the underwater propeller to generate thrust, and the aerial propeller free-wheels. The motor's rotation direction determines whether the one-way clutch engages or overruns, while tilting the propulsion unit changes the thrust direction. Compared with the dual-clutch, opposite-side layouts, this arrangement removes one clutch and the opposite-side transmission path, at the cost of driving the submerged aerial propeller during reverse WATER operation.

Table 2
Selected propulsion systems under the 600 mm footprint constraint.

Item	Tri-rotor	Quad-rotor
Motor	T-MOTOR V3115 KV900	T-MOTOR Cine66 2812 KV925
Propeller	T10.5 × 5-3	HQ9050-3
ESC	SkyWalker V2 6S	SkyWalker V2 6S
Motor mass (g)	113.1	76.4
Propeller mass (g)	26.5	17.4
ESC mass (g)	63	63
Max. thrust per rotor (kgf)	4.735	2.923
Max. power per rotor (W)	1894	1237.5

Taken together, under the specified 600 mm footprint and component database, the selected tri-rotor provides the more favourable aerial propulsion solution. It combines greater maximum thrust, lower hover power at the common gross mass, lower installation mass, and a higher theoretical payload allowance. These combined advantages motivated the selection of the tri-rotor layout for YingLong-T.

These results compare aerial propulsion subsystems under the stated footprint constraint, component database, and modelling assumptions; they do not establish a general advantage of tri-rotor vehicles or a performance advantage between matched triphibious prototypes. The calculated payload allowances are theoretical estimates, whereas YingLong-T demonstrated a payload of 0.85 kg in flight tests.

3.4. Unified powertrain and propulsion unit

Here, "unified powertrain" denotes reuse of the same three motor–ESC units, aerial–underwater propeller assemblies, and tilting mechanisms as the primary propulsion hardware in AIR, LAND, and WATER; it does not imply that every actuator is shared or that the hardware is individually optimal in each domain.

As shown in Fig. 3, each propulsion unit combines a waterproof vectoring mount, a bidirectional brushless motor, and a same-side aerial–underwater propeller assembly. An underwater propeller with a diameter of 70 mm is fixed directly to the motor shaft, whereas an aerial propeller with a diameter of 267 mm on the same side is coupled through a single one-way clutch. A waterproof dual-axis servo rotates the propeller assembly through 90° to redirect its thrust. The ESC receives separate PWM signals for throttle and rotation direction. The throttle pulse width ranges from 1050 to 1950 μs. For the direction signal, pulse widths above 1600 μs select one motor rotation direction, while those below 1400 μs select the opposite direction. The selected rotation direction determines whether the one-way clutch engages or overruns. In AIR and LAND, the clutch is engaged, so the motor drives the aerial propeller while the directly coupled underwater propeller co-rotates. In nominal forward WATER operation, the clutch overruns; the aerial propeller free-wheels while the motor drives the underwater propeller directly.

The clutch inner ring is fixed to the motor shaft, while its outer ring is fixed to the propeller clamp carrying the aerial propeller. The

clutch state therefore determines how motor-shaft torque is transmitted to the two propellers. For quasi-steady rotation, the motor-shaft torque balance is $Q_m \simeq Q_{uw} + Q_a + Q_{loss}$ when the clutch is engaged and $Q_m \simeq Q_{uw}+Q_{ov}$ when it overruns. Here Q_m is the torque delivered at the motor output shaft, Q_{uw} is the resisting torque of the directly coupled underwater propeller, Q_a is the resisting torque of the aerial propeller, Q_{loss} groups unmeasured parasitic torque from the rotating clutch and propeller-mount hardware in the engaged state, and Q_{ov} is the total clutch-drag torque acting on the motor shaft during overrunning. In AIR, LAND, and reverse WATER operation, the clutch locks the inner and outer rings together so that they rotate at the same speed. Motor-shaft torque is transmitted through the inner ring, outer ring, and propeller clamp to the aerial propeller. In forward WATER operation, the clutch overruns: the inner ring rotates with the motor shaft, while the outer ring, clamp, and aerial propeller can rotate independently of it. Clutch drag can still transmit torque to the aerial propeller, while relative rotation dissipates power in the clutch. Local water flow may also contribute to the aerial propeller's rotation. In both states, the underwater propeller remains directly driven by the motor shaft.

Motor reversal and one-way transmissions have previously been used to select medium-specific propellers in Dipper and Nezha-SeaDart III (Rockenbauer et al., 2021; Jin et al., 2026). Unlike their opposite-side, dual-clutch layouts, the YingLong-T propeller assembly places both propellers on the same side of a single-output-shaft motor, fixes the underwater propeller directly to the motor shaft, and couples the aerial propeller to the shaft through a single one-way clutch. This arrangement eliminates the second clutch and the opposite-side transmission path, shortens the axial package, and leaves the motor base unobstructed for direct attachment to the vectoring mount. The present ESC uses separate throttle and direction signals, whereas Nezha-SeaDart III encodes motor direction and throttle magnitude in a single neutral-centred PWM command. This distinction concerns command implementation rather than a claimed performance advantage. The motor shaft drives the underwater propeller directly, bypassing the one-way clutch and potentially reducing transmission losses. Unlike the water-exit sequence reported for Nezha-SeaDart III, which uses underwater propulsion before rapidly reversing the motor near the free surface (Jin et al., 2026), YingLong-T first reaches its positively buoyant surfaced equilibrium, where the elevated propeller placement keeps all blades above the free surface. Aerial propulsion is enabled only after this condition is met, avoiding powered blade passage through the air–water interface and the associated asymmetric unsteady loads, as well as abrupt motor reversal under load; its mechanism and guards are detailed in Section 5.2.

The propeller tests provide the experimental basis and operating limits for this single-clutch arrangement. In air, the co-rotating underwater propeller produced nearly unchanged thrust and only a small power and efficiency penalty under the tested conditions, supporting omission of a second clutch (Section 6.1.2). In forward underwater operation, the propeller assembly outperformed the underwater propeller alone, whereas reverse rotation engaged the clutch and imposed the large aerial propeller as an additional submerged load (Section 6.1.3). The design therefore favours the forward-dominant underwater mission while accepting reduced reverse performance.

3.5. Integrated electrical system

Fig. 4 shows the connections among the power supply, flight controller, sensors, communication modules, and actuators. The component representations (boxes, images, and text labels) and connection-line styles were informed by the diagrams in Jin et al. (2025, 2026), whereas the component selection and interconnection architecture are specific to YingLong-T. Table 3 lists the system components.

Table 3
Electronic components of YingLong-T.

Component	Model/Specification	Qty
Battery	Grepow 5000 mAh, 75C, 22.2 V (6S1P)	1
Power module	Holybro PM02 V3	1
UBEC	YZW high-voltage UBEC	1
Flight controller	Holybro Pixhawk 6C Mini	1
ESC	HOBBYWING SkyWalker V2, 60 A, 3–6S	3
Motor	T-MOTOR V3115, KV900	3
Type-I tilt servo	Ruosi waterproof dual-axis, 30 kgf cm, 270°	3
Type-II steering servo	LIEYING waterproof, 12 kgf cm, 270°	1
Relay	PWM-controlled relay	1
Electromagnet	LANGSODA LSD-0520B, 24 V	1
GPS	Holybro M9N	1
Depth sensor	VIOCEAN MS5837 M10	1
Radio telemetry	3DR X7, 433 MHz	2
RC transmitter	ELRS, 500 MHz	1
RC receiver	ELRS, 500 MHz	1
Remote controller	RadioMaster TX16S MKII	1

Power supply. A 6S 5000 mAh lithium-polymer battery supplies the nominal 22.2 V power through a Holybro PM02 module, which also measures battery voltage and current and regulates power for the flight controller. The main bus feeds the three ESCs, an 8.4 V UBEC, and the electromagnetic-brake circuit; the UBEC powers the three tilt servos and rear steering servo.

Control and actuation. A Pixhawk 6C Mini is the sole onboard controller in AIR, LAND, and WATER. It receives GPS, pressure-depth, RC, and telemetry inputs and directly commands the three ESCs, three tilt servos, rear steering servo, and brake relay. This removes inter-controller switching and reduces duplicated electronics, cabling.

The three motor–propeller assemblies and type-I servos form the unified powertrain. A separate type-II servo steers the rear caster. For braking, a PWM-controlled relay energizes a push–pull electromagnet that presses a friction pad against the rear wheel; a return spring releases the pad when power is removed.

Communication. A 500 MHz ELRS link carries operator commands, and paired 433 MHz radios provide bidirectional MAVLink telemetry. These sub-GHz links were chosen to reduce freshwater attenuation relative to commonly used GHz-band radios (Liu et al., 2023). They are prototype-development links, not an operational marine communication solution. Both remained functional to a maximum tested depth of 2.5 m in one freshwater condition; this observation does not establish general depth, range, reliability, or seawater performance.

4. Multi-domain control implementation

YingLong-T reuses the same three propulsion units in AIR, LAND, and WATER. Switching between these domains requires the single firmware to select the appropriate controller and state feedback, load the corresponding control gains and limits, and update the actuator allocation and motor-direction rules while preventing conflicting commands from reaching the shared hardware. Within each domain, the control mode (e.g., STABILIZE or ALT_HOLD) determines how commands are interpreted and which feedback control loops are active.

4.1. ArduPilot-based single-firmware integration

As shown in Fig. 5, the implementation retains a single ArduPilot runtime for scheduling, hardware abstraction and sensor drivers, RC/MAVLink communication, parameter management, arming and failsafe handling, state estimation, logging, and low-level output services. Raw sensor data are processed through this common runtime; no domain-specific controller accesses hardware drivers directly.

Within this shared runtime, the AIR and WATER controller adapters encapsulate selected control functions derived from ArduCopter and

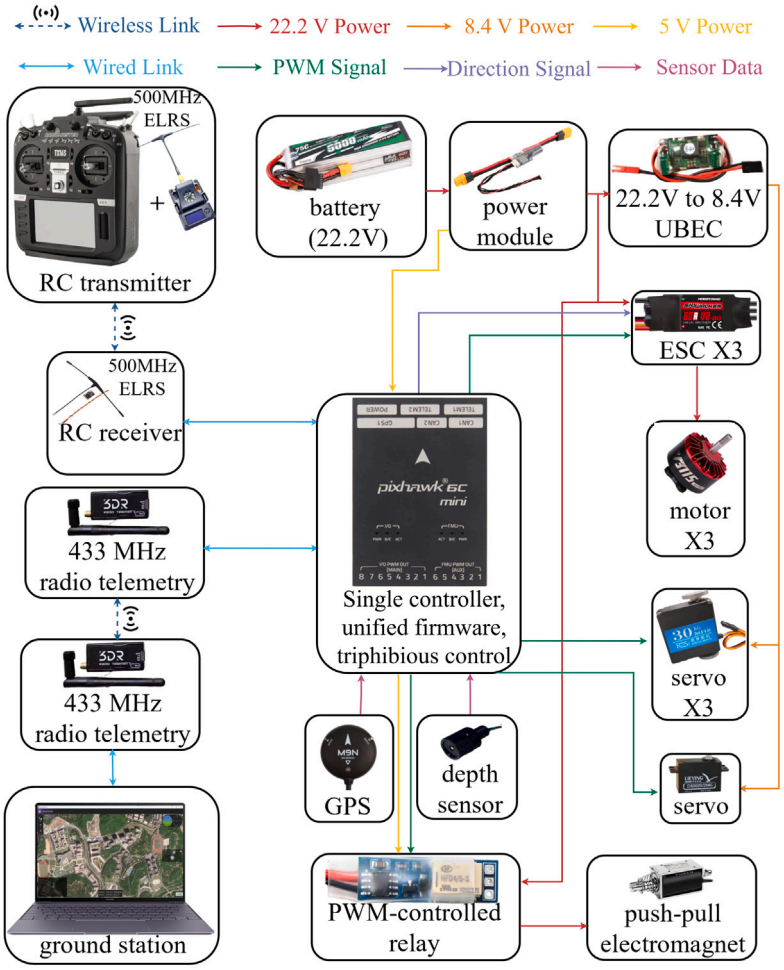


Fig. 4. Integrated electrical system for shared power distribution, sensing, communication, and actuation across AIR, LAND, and WATER. A single battery supplies the propulsion and regulated electronics/servo power branches, while one Pixhawk 6C Mini receives RC, telemetry, and sensor inputs and commands propulsion, tilting, steering, and braking. This integration avoids separate control boards and power sources for each mobility domain.

ArduSub, respectively. The corresponding allocation functions, derived from AP_Motors, are integrated into the Domain-Aware Actuator Interface. The custom LAND controller adapter follows the same interface convention, passing its control demands to the actuator interface for allocation and output. The Domain Context Switchboard prepares the parameter profile, state feedback, and controller context for the requested domain before activation.

Input commands are handled according to their function. Requests to switch between AIR, LAND, and WATER are routed to `YLT_DomainManager`, while commands to change the control mode within the active domain are handled by its controller adapter. Continuous stick inputs and mission setpoints provide control targets to the active adapter. This separation ensures that a control-mode change does not itself trigger a mobility-domain switch, which must follow the guarded transition procedure. Arming and failsafe states are managed globally across all domains.

The State and Health Monitor evaluates estimator validity, required-driver health, failsafe flags, and commanded-output status. It provides guard conditions to the DomainManager and a safety-inhibit signal to the actuator interface. The inhibit can suppress outputs but cannot select a domain or authorize a controller, leaving the DomainManager as the sole domain authority.

After domain-dependent allocation, saturation and slew-rate limiting, and logical-function routing, normalized actuator commands are passed to `SRV_Channels`, which applies channel range, trim, and reversal calibration. `AP_HAL::RCOutput` then generates the configured board-level signals. Thus, the customized layer determines actuator function and commanded state, while the retained ArduPilot services perform final channel calibration and hardware output. This single-runtime organization also avoids duplicated controllers as well as inter-controller handover, while providing a common time base for sensing, command generation, output, and logging.

4.2. Mobility-domain supervision and context switching

The `YLT_DomainManager` maintains the active domain

$$D = \{\text{AIR}, \text{LAND}, \text{WATER}\}. \tag{7}$$

A request is first validated and arbitrated among the RC link, ground control station, and mission logic according to a predefined priority policy. An accepted request remains pending until the entry, health, and output-interlock conditions are satisfied. Section 5.3 gives the domain-specific guards and thresholds.

An admitted request starts an internal finite-state machine. The DomainManager gates the outgoing controller demand, holds propulsion at zero or neutral, commands the target tilt-servo trajectory with bounded slew rates, and requests preparation of the control context for the target domain. Motor direction can change only after a zero or neutral propulsion command has been established. Because the prototype has no tilt-servo position feedback, reorientation is verified only at the

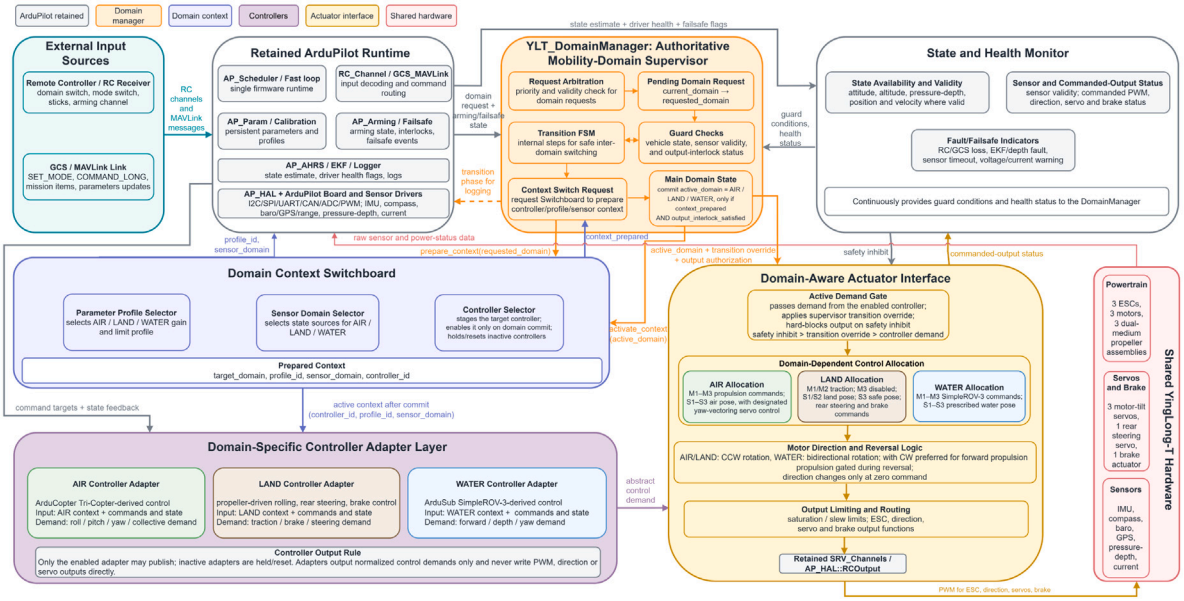


Fig. 5. ArduPilot-based single-firmware architecture for coordinating AIR, LAND, and WATER on a single flight controller. The retained runtime provides common sensing, estimation, communication, failsafe, and logging services. The YLT_DomainManager authorizes domain changes using State and Health Monitor checks, while the Domain Context Switchboard prepares the required parameters and controller context. Only the active controller adapter supplies demands to the Domain-Aware Actuator Interface, which allocates and routes all actuator commands. This architecture reuses common runtime services across all three domains to reduce software duplication and routes actuator commands through a single interface to prevent conflicting outputs.

command level through the target command and a prescribed settling interval; physical servo position is not claimed to be measured.

The Switchboard performs a prepare–commit handover. During preparation, it prepares the target gain and limit profile, state feedback, and controller adapter, while inactive controller is held to prevent stale integrator states from being published. A prepared controller cannot publish outputs. The DomainManager commits the new domain only after receiving `context_prepared` and confirming the command-level output interlock. Context activation and domain commitment occur atomically in the scheduler sequence, after which only the newly active adapter may publish demands. This procedure prevents partial switching, such as applying a new allocation with an old parameter profile or enabling a controller before the preceding propulsion command has been removed.

4.3. Domain-specific controller adapters

Once a domain has been committed, its controller adapter receives command targets and the required state feedback from the shared runtime and operates with the parameter profile activated by the Switchboard. All adapters export a common form of normalized control demand; none writes PWM values or addresses actuator channels directly.

The AIR adapter follows the ArduCopter tri-copter structure. An outer attitude P loop generates angular-rate targets, and an inner rate PID loop with feedforward produces roll, pitch, and yaw demands. Altitude and position loops are invoked only by the within-domain modes that require them. These demands and the collective-thrust command are allocated among the three motors and the yaw-vectoring tilt servo. The control loops are conventional; their role here is integration with the common supervision and output-ownership framework.

The LAND adapter controls propeller-driven rolling. The two front propulsion units provide traction through the aerial propellers, while passive wheels support the body, a servo-steered rear caster controls heading, and an electromagnetic brake decelerates the vehicle. Because the passive wheels provide no wheel-speed measurements, the controller does not assume wheel odometry and instead uses available IMU- and GPS-derived motion information where valid. Traction–brake arbitration prevents simultaneous contradictory commands.

The WATER adapter is derived from the ArduSub SimpleROV-3 architecture (ArduPilot Development Team, 2026) and provides forward, depth, and yaw control channels, denoted by F, Z, and Y, respectively. The two horizontal propulsion units (M1/M2) receive a common forward component and opposite-sign yaw components, while the vertical unit (M3) receives the depth-channel command as vertical thrust. No hull-specific hydrodynamic parameters enter the implemented control laws. In the WATER configuration, roll, pitch, and lateral motion are not independently controlled. The centre of mass lies below the centre of buoyancy, providing restoring moments that help stabilize roll and pitch passively.

The adapter outputs are

$$\mathbf{u}_{\mathrm{AIR}} = [u_{\mathrm{roll}}, u_{\mathrm{pitch}}, u_{\mathrm{yaw}}, u_{\mathrm{collective}}]^T, \tag{8}$$

$$\mathbf{u}_{\mathrm{LAND}} = [u_{\mathrm{traction}}, u_{\mathrm{brake}}, u_{\mathrm{steering}}]^T, \tag{9}$$

$$\mathbf{u}_{\mathrm{WATER}} = [u_{\mathrm{forward}}, u_{\mathrm{depth}}, u_{\mathrm{yaw}}]^T. \tag{10}$$

AIR roll, pitch, and yaw demands, WATER forward and yaw demands, and LAND steering demands are normalized to $[-1, 1]$. AIR collective, WATER depth, and LAND traction and brake demands use $[0, 1]$. For the WATER depth channel, 0.5 denotes neutral thrust; the demand is converted to a signed vertical-thrust command in $[-1, 1]$ before motor mixing. The Domain-Aware Actuator Interface mediates all subsequent access to the shared hardware.

4.4. Domain-aware actuator interface

The Domain-Aware Actuator Interface converts the accepted adapter demand into commands for the three ESCs, three motor-tilt servos, rear steering servo, and brake actuator. Its active-demand gate enforces the following precedence:

$$\mathbf{a}_{\mathrm{cmd}} = \begin{cases} \mathbf{a}_{\mathrm{safe}}, & s_{\mathrm{inhibit}} = 1, \\ \mathbf{a}_{\mathrm{transition}}, & s_{\mathrm{inhibit}} = 0 \wedge q_{\mathrm{transition}} = 1, \\ \mathcal{A}_d(\mathbf{u}_d), & \text{otherwise.} \end{cases} \tag{11}$$

Here, s_{inhibit} denotes the safety-inhibit flag issued by the monitor, $q_{\text{transition}}$ indicates whether a transition is active, and $d = d_{\text{active}} \in \mathcal{D}$ denotes the currently active domain. $\mathbf{a}_{\text{safe}}$ and $\mathbf{a}_{\text{transition}}$ contain the predefined safe actuator commands and the supervisor-authorized transition actuator commands, respectively. $\mathcal{A}_d(\cdot)$ maps the control demands of the active domain to actuator commands. The selected actuator-command vector then undergoes amplitude and rate limiting, channel calibration, and routing to the hardware outputs.

In AIR, the tri-copter allocation converts roll, pitch, yaw, and collective thrust demands into commands for the three motors and the aft yaw-vectoring servo. In LAND, traction commands are applied to the two front motors, the aft motor is disabled, and steering and braking commands are sent to their respective actuators. In WATER, the SimpleROV-3-derived allocation combines forward and yaw demands to command the two front motors and maps the depth demand to the aft motor. In addition to control allocation, the actuator interface maintains the propulsion-unit orientations required by the active domain, while allowing the aft unit to tilt for yaw control in AIR. These domain-specific configurations are detailed in Section 5.1.

The interface reports the output PWM commands for motor throttle, motor rotation direction, servo position, and brake actuation to the State and Health Monitor for interlocking, diagnostics, and logging. These values represent the issued commands rather than measured actuator responses.

This architecture integrates ArduCopter-derived aerial control, custom terrestrial control, and ArduSub-derived underwater control within a single ArduPilot runtime, using one actuator interface to command the shared reconfigurable powertrain. The domain supervisor, context-switching mechanism, and actuator interface keep the active controller, parameter profile, state feedback, actuator allocation, and motor rotation directions consistent with the active domain during operation and domain switching.

5. Domain-specific configuration and cross-domain transition control

This section complements the single-firmware implementation in Section 4 by specifying the actuator poses, physical transition mechanism, entry guards, and completion criteria for domain switching.

5.1. Domain-specific configuration

Fig. 6 and Table 4 summarize the configuration in each mobility domain. Servos 1 and 2 rotate the front propulsion units by 90° between the AIR and LAND/WATER poses; servo 3 vectors the aft unit for aerial yaw control, and servo 4 steers the rear wheel in LAND. Thus, the tri-rotor, three-wheel, and Y3 arrangements reuse the same three propulsion units and triangular body rather than forming independent locomotion modules.

5.2. Mechanistic basis of the buoyancy-assisted air–water transition

The air–water transition is deliberately staged and assisted by positive buoyancy rather than treated as an instantaneous switch. Propulsion remains off while a propeller is partially immersed, avoiding operation across the air–water surface. Taking upward as positive, the dominant vertical-force and pitch-moment relations are

$$m\ddot{z} = B(z,\phi,\theta) - W - D_z + \sum_i T_{i,z}, \tag{12}$$

$$I_y\dot{q} = M_{\text{B}} + M_{\text{T}} + M_{\text{h}}, \tag{13}$$

where B, W, and D_z denote buoyancy, weight, and vertical hydrodynamic resistance, respectively; $T_{i,z}$ is the vertical component of the ith propulsion force; and M_{B}, M_{T}, and M_{h} denote the pitch moments about the vehicle's centre of mass due to buoyancy, propulsion forces, and other hydrodynamic effects, respectively. These relations describe the dominant mechanism rather than a coupled free-surface model. They were not used to design or run the implemented controller.

For AIR–WATER operation, reorienting motors 1 and 2 moves their mass rearward and produces a nose-up floating attitude in which the underwater propellers driven by motors 1 and 2 become immersed before motor 3. Their reverse thrust then drives the vehicle backward and downward into the water. Its vertical component overcomes net positive buoyancy and vertical hydrodynamic resistance, while its horizontal component overcomes horizontal hydrodynamic resistance.

For WATER–AIR operation, stopping underwater propulsion leaves $B - W > 0$ while the vehicle is submerged, producing a passive ascent towards the designed floating equilibrium. The corresponding propeller-clearance requirement is

$$c_{\text{p}} := z_{\text{tip,min}} - z_{\text{water}} > 0.05\,\text{m}. \tag{14}$$

With the 0.85 kg payload, the measured minimum vertical clearance in the static surfaced configuration satisfied this requirement. The propellers may cross the free surface during passive emergence but remain unpowered throughout emergence and reconfiguration; aerial propulsion is enabled only after stable surfacing has been confirmed, the AIR-entry guards are satisfied, and the AIR domain has been committed.

5.3. Guarded domain-switching logic and completion criteria

The implemented transition graph supports bidirectional AIR–LAND and AIR–WATER transitions. Transitions between LAND and WATER must pass through AIR because the wheeled configuration cannot reliably traverse soft or uneven shorelines. Let d be the pressure-derived depth relative to the water surface, with $d = 0$ at the surface and negative downward. Fig. 7 summarizes the guarded transition logic, and Table 5 lists the associated thresholds and timing parameters.

The AIR-entry attitude guard is

$$g_{\text{A}} = \left(|\phi| \le \phi_{\max,\text{A}}\right) \wedge \left(|\theta| \le \theta_{\max,\text{A}}\right) \wedge \left(\|\boldsymbol{\omega}\|_2 \le \omega_{\max,\text{A}}\right). \tag{15}$$

The domain-specific entry guards are

$$g_{\text{A2L}} = \texttt{DISARMED}, \tag{16}$$

$$g_{\text{A2W}} = \texttt{DISARMED} \wedge (d \le d_{\text{W}}), \tag{17}$$

$$g_{\text{L2A}} = \texttt{DISARMED} \wedge g_{\text{A}}, \tag{18}$$

$$g_{\text{W2A}} = \texttt{DISARMED} \wedge \left(|d - d_{\text{eq}}| \le \Delta d_{\text{surf}}\right) \wedge g_{\text{A}}. \tag{19}$$

Each is combined with the common health guard g_{H}:

$$g_{X2Y}^{\text{entry}} = g_{\text{H}} \wedge g_{X2Y}. \tag{20}$$

As described in Section 4.2, g_{H} requires valid transition-relevant sensor and state estimates, no active failsafe or safety inhibit, and valid commanded-output status. A violation rejects the request or aborts an active transition. The complete entry condition must remain true for T_{g}, filtering transient threshold crossings. For WATER–AIR entry, this interval confirms both the surfaced-depth band and the AIR attitude limits.

After admission, the protected finite-state machine described in Section 4.2 holds all motors at zero while S1/S2 move to the target pose and the target domain context is prepared. Because the tilt servos have no position feedback, pose completion is inferred from the command and the settling delay T_{s}, not measured directly. The DomainManager commits the target domain only when `context_prepared` is true and T_{s} has elapsed; target-domain propulsion can be enabled only after this commitment.

Let $X, Y \in \mathcal{D} = \{\text{AIR}, \text{LAND}, \text{WATER}\}$, with $X \neq Y$, denote the source and target domains, respectively. The binary variable $S_{X\to Y}$ indicates whether the requested domain switch has been completed:

$$S_{X\to Y} = \begin{cases} 1, & \left(D_{\text{active}} = Y\right) \wedge \left(c_{\text{active}}(Y) = 1\right) \wedge \left(q_{\text{transition}} = 0\right), \\ 0, & \text{otherwise.} \end{cases} \tag{21}$$

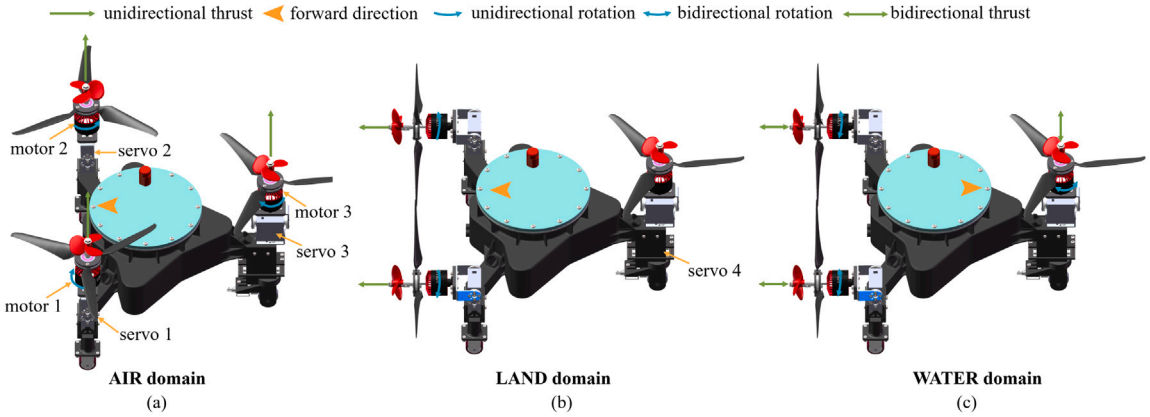


Fig. 6. Cross-domain reconfiguration of the three shared propulsion units: (a) AIR, with three lifting units and aft thrust vectoring for yaw control; (b) LAND, with two horizontal front units propelling the vehicle on passive wheels; and (c) WATER, with two horizontal front units for surge and differential-thrust yaw control and a vertical aft unit for depth regulation. Reusing these units avoids dedicated wheel-drive motors and a separate underwater-thruster set. Direction conventions and detailed actuator configurations are given in Table 4.

Table 4
Domain-specific actuator settings, motor rotation, and thrust directions.

Domain	Servo settings and propulsion-unit orientation	Motor rotation and vehicle thrust	Enabled controller adapter
AIR	S1/S2: 0°, with the front units vertical. S3 varies about 0° to tilt the aft unit for yaw control. S4: 0°, neutral steering.	M1: CW; M2: CCW; M3: CW. All three units provide lift; tilting M3 adds a thrust component for yaw control.	AIR adapter
LAND	S1/S2: 90°, with the front units horizontal. S3: 0°, with the aft unit vertical. S4 varies about 0° for rear-wheel steering.	M1: CW; M2: CCW, producing thrust in the LAND forward direction. M3 is disabled.	LAND adapter
WATER	S1/S2: 90°, with the front units horizontal. S3: 0°, with the aft unit vertical. S4: 0°, neutral steering.	M1 CCW/M2 CW: forward thrust. M1 CW/M2 CCW: reverse thrust. M3 CCW: downward thrust; M3 CW: upward thrust.	WATER adapter

Mi and Si denote motor i and servo i, respectively. CW/CCW rotation is viewed from the propeller side along the motor shaft towards the motor. Front and aft are fixed mounting positions referenced to the AIR/LAND body-forward direction; forward motion in WATER is opposite to this direction. Thrust directions refer to forces acting on the vehicle in each nominal domain configuration.

Table 5
Variables and parameters used in the transition logic.

Symbol	Definition	Value
d (m)	Pressure-derived depth, negative downward	Measured
T_s (s)	Prescribed delay for open-loop servo reconfiguration	0.4
T_g (s)	Continuous confirmation time applied to every transition-entry guard	0.4
d_W (m)	Depth threshold for WATER-domain entry	−0.10
d_{eq} (m)	Pressure-sensor depth at the stable surfaced equilibrium	−0.15
Δd_{surf} (m)	Allowable depth deviation for WATER-to-AIR entry	0.03
d_{imm} (m)	Depth at which motor 3 is fully immersed	−0.25
$\phi_{max,A}, \theta_{max,A}$ (°)	AIR-entry roll and pitch limits	5
$\omega_{max,A}$ (°/s)	AIR-entry angular-rate limit	10

Here, D_{active} is the domain committed by the DomainManager, $c_{active}(Y)$ is a Boolean variable indicating that the prepared parameter, sensor, and controller context of domain Y has been activated, and $q_{transition}$ indicates whether the transition FSM is active. This criterion does not include the subsequent physical task.

5.4. Staged surface submergence

After the AIR-to-WATER domain switch, motors 1 and 2 generate reverse thrust to initiate submergence from the nose-up floating configuration described in Section 5.2. Motor 3 is held at zero command while it remains exposed to air or partially immersed. When the measured depth reaches d_{imm}, motor 3 is considered fully immersed and is enabled to provide vertical thrust for depth regulation. Motors 1 and 2 then switch to CCW and CW rotation, respectively (Table 4), to provide forward thrust with their one-way clutches overrunning. The vehicle subsequently uses this more efficient forward-propulsion configuration for underwater motion.

6. Experimental evaluation and discussion

The experimental programme evaluated integrated propeller performance, vehicle performance within each mobility domain, and complete cross-domain transition sequences. Bench tests were followed by AIR, LAND, and WATER vehicle tests and by cross-domain cycles in a pool, a river, and a coastal-aquaculture environment. The relevant test conditions and statistical treatment are stated in each subsection; supplementary videos provide additional vehicle-level evidence.

6.1. Integrated propeller performance

6.1.1. Propeller performance test setup

Fig. 8 shows the common test stand, and Table 6 lists components not already reported in Table 3. A force gauge measured aerial thrust

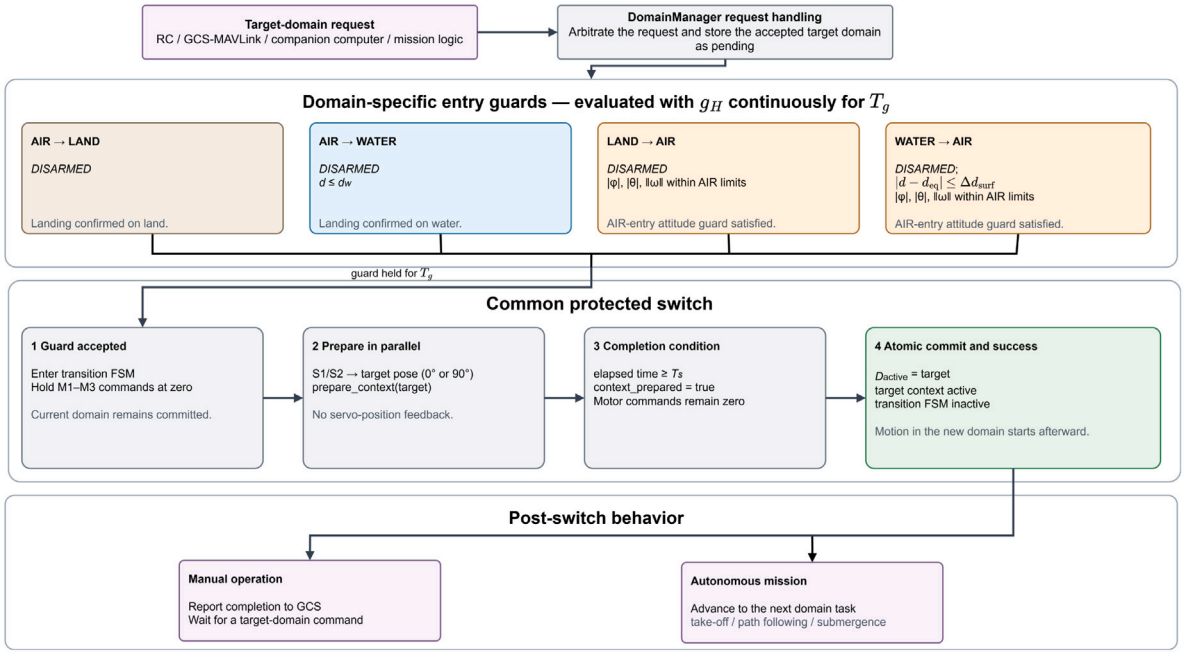


Fig. 7. Guarded domain-switching logic. Requests are admitted after the entry and health guards remain satisfied for T_g. Motors remain at zero while the S1/S2 pose and domain context are prepared. The target domain is committed once T_s has elapsed and context preparation is complete; target-domain propulsion can be enabled only after this commitment, preventing partial activation and inconsistent outputs.

directly. Underwater thrust was inferred from the torque measured above the waterline and the known lever arm of the aluminium-tube mount. ESC telemetry provided rotational speed, voltage, current, temperature, and energy data, while the flight controller and Mission Planner recorded the throttle command.

Throttle was increased from zero to maximum in approximately equal increments and held for 3 s at each setting. Three smartphones recording at 30 fps—one capturing the remote controller display, one capturing the force/torque readout, and one capturing the propeller in operation—stream to the computer running Mission Planner, where all feeds are displayed alongside the throttle readout on a single screen and captured via screen recording.

For each throttle plateau, the timestamps marking the end of the throttle adjustment and the beginning of the next adjustment were identified. The midpoint between these timestamps was used as the centre of the sampling window. 15 data points closest to the midpoint were extracted at two-frame intervals, corresponding to a sampling interval of approximately 0.067 s and a total window of approximately 0.93 s at 30 fps. These samples were averaged to obtain one trial-level value for each throttle setting. All propeller configurations were tested using the same motor, ESC, mounting geometry, and measurement procedure. The battery was fully charged to 25.2 V before each trial. For the underwater tests, the propeller was fully submerged to a depth of 250 mm below the water surface. Unless otherwise stated, each propeller configuration under each operating condition was tested in three independent throttle sweeps across the full throttle range. Thrust, rotational speed, voltage, and current were recorded simultaneously.

6.1.2. Aerial thrust tests

Four configurations were compared (Fig. 9): the aerial propeller with the original hub, the aerial propeller with the integrated hub, the isolated underwater propeller, and the integrated propeller. Fig. 10 reports the mean values from three independent throttle sweeps. The larger integrated hub increased the effective aerial-propeller diameter and produced higher thrust than the original-hub configuration throughout the tested range.

Table 6
Components used in the propeller-performance tests.

Component	Model/Specification	Qty
Receiver	FrSky X8R 2.4 GHz	1
Remote controller	FrSky X9D Plus	1
ESC	FLYCOLOR Xcross HV3	1
Force gauge	Mayatech MT5(resolution: 1 gf)	1
Torque sensor	SBT850A(resolution: 0.15 N m)	1
Transmitter	SBT904	1

To assess the aerial performance penalty associated with underwater-propeller co-rotation, we compared the integrated propeller with the aerial propeller using the same integrated hub. Adding the underwater propeller left aerial thrust nearly unchanged and caused only a small increase in electrical input power. The corresponding reduction in the thrust-to-input-power ratio remained within 0.5 gf/W over the tested range. These results support retaining direct drive of the underwater propeller during AIR operation. We accept this small measured aerial penalty in exchange for the simpler single-clutch arrangement described in Section 3.4: only the aerial propeller is coupled through a one-way clutch, avoiding a second clutch and the associated transmission components needed to disengage the underwater propeller.

6.1.3. Underwater thrust tests

The test was conducted in a water tank (4.0 × 2.0 × 1.0 m). The integrated assembly and the isolated aerial and underwater propellers were tested fully submerged for both clockwise (CW) and counter-clockwise (CCW) motor rotation (Fig. 11). The aerial propeller alone generated negligible thrust in either direction, confirming that it cannot serve as the primary underwater propulsor.

For the tested integrated assembly, CW motor rotation causes the clutch to overrun, allowing the aerial propeller to free-wheel while the motor directly drives the underwater propeller. The integrated assembly outperformed the isolated underwater propeller over the tested points. At 40% throttle, it generated approximately 11% more thrust with 9% less input power, corresponding to an approximately

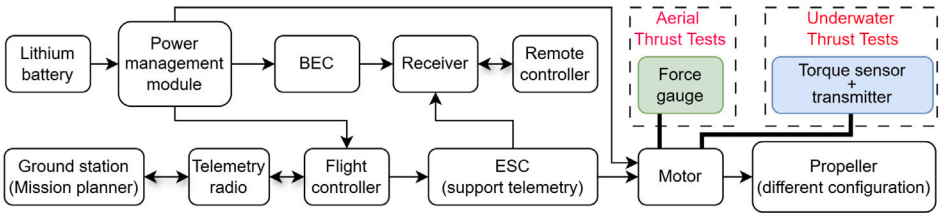


Fig. 8. Propeller-performance test setups: aerial thrust is measured directly with an axial force gauge, whereas underwater thrust is inferred from above-water torque and the known lever arm. ESC telemetry and synchronized video record throttle, rotational speed, voltage, current, and power. All configurations use the same motor, ESC, mounting geometry, and sampling procedure.

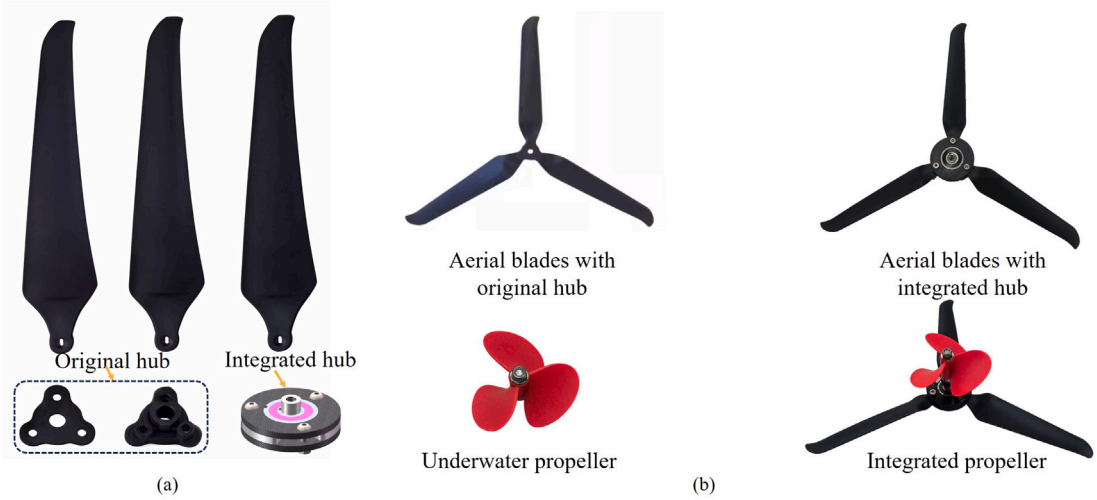


Fig. 9. Propeller test configurations: (a) blades and two hub types; (b) four test assemblies.

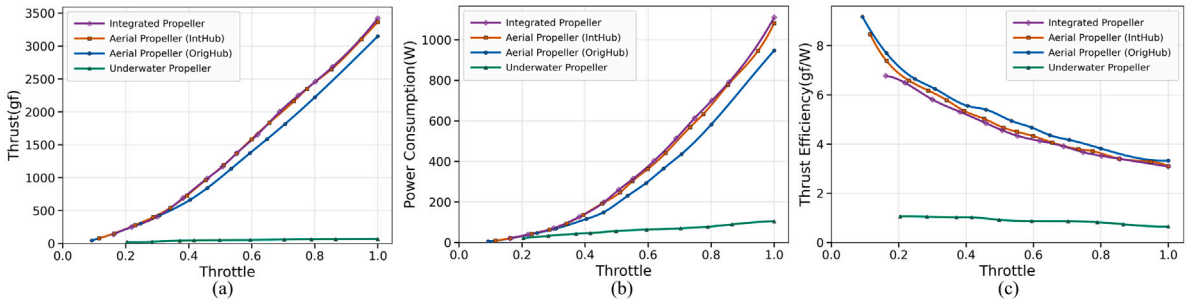


Fig. 10. Static propeller performance in air versus throttle: (a) thrust, (b) electrical input power, and (c) thrust-to-input-power ratio. Comparisons include the integrated propeller, the aerial propeller with the integrated hub (IntHub) or original hub (OrigHub), and the isolated underwater propeller. Relative to the aerial propeller with the same integrated hub, adding the underwater propeller changes thrust little and reduces the thrust-to-input-power ratio by no more than 0.5 gf/W over the tested range, supporting direct coupling of the underwater propeller without a second clutch.

22% increase in thrust-to-input-power ratio. A plausible explanation is beneficial pre-rotation: the freely rotating upstream aerial blades may modify the local inflow while avoiding the resistance of a locked propeller, potentially improving the effective angle of attack at the underwater-propeller blades (Zheng et al., 2026). This interpretation was not isolated experimentally and is therefore treated as a mechanistic hypothesis.

In CCW motor rotation, the clutch engages and the motor must rotate both blade sets in water. The large-diameter aerial blades plausibly add substantial underwater torque load, consistent with the low speed and thrust of the integrated assembly under CCW rotation; this contribution was not measured separately. The resulting asymmetry is an architectural trade-off: the simpler single-clutch propeller assembly preserves aerial performance and favours the forward-dominant underwater inspection task at the expense of reverse propulsion authority.

6.2. Aerial flight performance

Outdoor manual-attitude-control tests assessed flight stability and payload capability; position–velocity cascade tracking and autonomous waypoint flight were not enabled. Two independent flights were conducted under each of two conditions: without payload and with an 850 g payload in clear weather with wind below 1.6 m/s. The battery was charged to 25.2 V before each flight, and onboard data were logged at 100 Hz. Because manual manoeuvre timing and duration differed, the trials were not averaged pointwise. The longer flight in each condition was selected to show a complete descriptive record, not to represent across-trial statistics. Fig. 12 shows the unloaded demonstration, and Fig. 13 compares the two selected records.

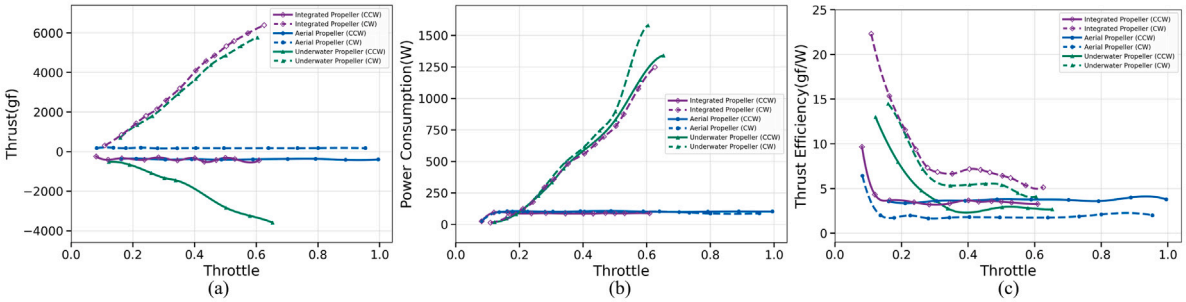


Fig. 11. Fully submerged propeller performance versus throttle: (a) thrust, (b) electrical input power, and (c) thrust-to-input-power ratio. The integrated propeller is compared with the isolated aerial and underwater propellers under CW and CCW motor rotation. For the tested propulsion unit, these rotation directions correspond to forward and reverse underwater propulsion, respectively. At approximately 40% throttle under CW motor rotation, the integrated propeller produces 11% more thrust with 9% less input power than the isolated underwater propeller, giving a 22% higher thrust-to-input-power ratio. Under CCW motor rotation, clutch engagement drives both propellers and the integrated propeller provides limited thrust, showing the trade-off associated with the single-clutch design.



Fig. 12. Unloaded aerial flight demonstration: (a) ground view, (b) onboard view, (c) map-based display of vehicle position and heading, and (d) flight trajectory; (a)–(c) are synchronized.

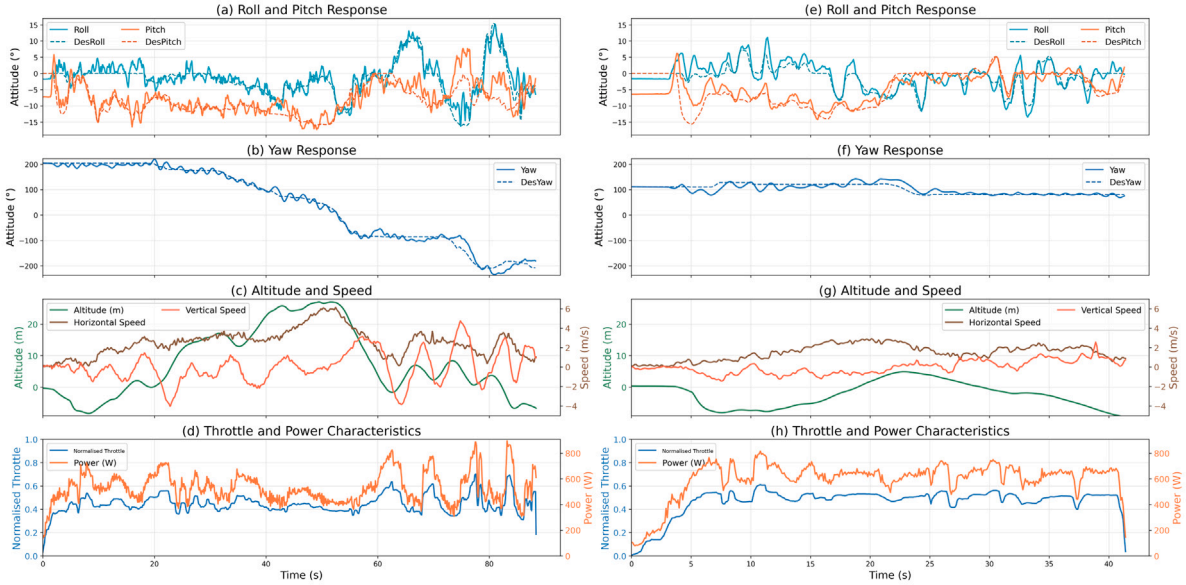


Fig. 13. Selected manual-flight records without payload (a–d) and with an 850 g payload (e–h): (a,e) roll and pitch tracking; (b,f) yaw tracking; (c,g) altitude and horizontal and vertical speeds; and (d,h) throttle command and electrical input power.

6.2.1. *Attitude response*

In the selected unloaded flight, roll tracking showed little visible delay and generally remained within 5° of the command. Pitch tracking was slower, with errors generally within 5° but occasionally exceeding 10° during aggressive manoeuvres, consistent with the longitudinal mass asymmetry. Yaw responded most slowly because it depends on coordinated differential thrust and aft-servo vectoring. The selected payload record showed similar qualitative responses on all three axes, demonstrating stable manual flight with the tested 850 g payload, but not establishing a maximum payload.

6.2.2. *Speed and endurance*

The selected unloaded flight reached horizontal, climb, and descent speeds of 6.2, 4.8, and 4.1 m/s, respectively. Its peak altitude of 27 m reflects the test trajectory rather than an operational ceiling. With the 850 g payload, the corresponding maxima were approximately 3.0,

2.7, and 1.5 m/s; altitude was intentionally restricted to below 5 m. The reduction reflects both the smaller thrust margin and conservative manual piloting, whose contributions were not separated.

During the steady-hover segments, the mean throttle and electrical power were approximately 0.44 and 520 W without payload, compared with 0.51 and 642 W with the 850 g payload. Although the total mass increased by 34%, the hover power increased by only 23%. Consequently, taking vehicle weight as the required steady-hover thrust, the estimated thrust-to-input-power ratio increased from 4.8 gf/W without payload to 5.2 gf/W with payload, indicating more thrust per unit of electrical input power at the higher loading condition. With a 6S 5000 mAh battery and a 10% landing reserve, these powers imply capacity-based endurance estimates of 11.5 and 9.3 min. These values are capacity-based estimates rather than measured endurance results.

6.3. Terrestrial mobility evaluation

Terrestrial tests were performed under dry conditions on a flat indoor terrazzo floor to assess tracking, speed, power, and turning radius. The results therefore do not characterize wet, uneven, or deformable terrain.

6.3.1. Trajectory tracking

The reference path combined a straight segment, a 120° turn, and a figure eight. An eight-camera NOKOV motion-capture system (±0.1 mm stated accuracy, 200 Hz) tracked four markers on the vehicle. Fig. 14 shows the setup and four independent trials. For each trial, planar tracking error was the Euclidean distance between measured and reference positions at the same sample index. The four trial-level RMSE values were 45.6 ± 23.6 mm (range: 26.8–80.1 mm), and the largest instantaneous error across all trials was 126.0 mm.

Trial 1 had the RMSE closest to the four-trial mean and was selected for the time histories in Fig. 15(a)–(b). During the displayed trial, the yaw remained stable along the straight segment (T_0–T_1) and varied smoothly during the 120° turn (T_1–T_2) and the figure-eight phase (T_3–T_8), with no abrupt oscillations, illustrating stable heading behaviour along the predefined path. These traces illustrate the representative trial; the RMSE statistics provide the across-trial result.

6.3.2. Speed and power characterization

Throttle was varied from 20% to 100% in 10-percentage-point increments, with three runs per setting. After accelerating along a straight approach corridor under the prescribed throttle command, the vehicle maintained stable speed for 2 s before entering a 7 m motion-capture region. Speed and power over the traversal were averaged to give one trial-level value; the averaging duration therefore varied with speed. In each run, settings were tested in ascending order, with the battery recharged between the 20%–70% and 80%–100% groups. Means and sample standard deviations were then calculated from the three trial-level values.

As shown in Fig. 15(c), mean speed rose from 1.10 ± 0.04 m/s at 20% throttle to 6.02 ± 0.08 m/s at 100%, while mean power rose from 32.0 ± 2.0 to 1150.0 ± 44.9 W. The maximum observed speed was 6.1 m/s. At the 20% operating point, the mean power and nominal battery energy, with a 10% reserve, imply a capacity-based endurance of approximately 187 min. This is an estimate rather than a measured run time and applies only to the tested flat surface and power point. These results demonstrate a wide speed range and low-power cruising capability on the tested flat surface.

6.3.3. Minimum turning radius

Turning radius was measured at 20% throttle and the mechanical steering limit of 68°; speed was not recorded. Pigment on the steered tyre marked its circular path. Three diameters at different orientations were averaged in each run, and their mean was halved. Three trials produced radii of 278, 280, and 297 mm, or 285 ± 10.4 mm (range: 278–297 mm). Steering clearance and tyre slip likely contributed to the variation.

Table 7
Peak angular velocities and accelerations in the representative trials shown in Fig. 17.

Manoeuvre	Axis	ω_{max} (°/s)	ω_{min} (°/s)	α_{max} (°/s²)	α_{min} (°/s²)
In-place 180° rotation	Yaw	11.7	−101.5	250.9	−267.7
Right-angle turn in Z-shaped navigation	Yaw	77.1	−94.3	213.3	−223.8
Diving–depth-keeping–surfacing	Pitch	36.2	−28.0	120.6	−143.0

6.4. Underwater manoeuvrability and depth regulation

All tests were conducted in an outdoor swimming pool (50.0 × 21.0 m) under calm, windless conditions. Water depth ranged from 1.5 to 2.2 m, and the bottom remained visible.

6.4.1. Speed characterization

Surface and submerged speeds were measured at 25%, 50%, 75%, and 100% throttle, with three runs per throttle–condition combination. The battery was recharged before each throttle-level group, and submerged runs used a depth of approximately 0.5 m. After a 10 m acceleration distance, the vehicle traversed a 15 m section marked at 0, 2, 4, 6, 10, and 15 m. Overhead 4 K video at 60 fps provided marker-passage times; steady segment speeds were averaged to obtain one trial-level value.

Fig. 16 reports the mean and sample standard deviation across the three runs. Speed increased with throttle and was higher when submerged at every tested setting. At 100%, mean surface and submerged speeds were 0.60 ± 0.01 m/s (range: 0.59–0.61 m/s) and 1.20 ± 0.03 m/s (range: 1.18–1.23 m/s), respectively. The steeper submerged speed–throttle trend indicates a greater speed response to throttle underwater. The lower surface speed is consistent with propeller ventilation, air entrainment, and wave-making losses near the free surface, although these contributions were not measured separately.

6.4.2. Manoeuvring agility

The manoeuvring tests included right-angle turns, in-place rotations, diving, and surfacing. The manually controlled in-place rotation was repeated three times, with completion measured from the onset of yaw change until the accumulated change reached 180° ± 5°. The mean duration was approximately 2.5 s, and the trial closest to this mean was selected for display. Multiple right-angle turns within one Z-shaped-navigation trial had a mean duration of approximately 1.5 s. Diving and surfacing were not timed, and their displayed response was taken from one depth-holding trial.

Attitude and angular-rate data were obtained from the onboard logs; yaw and pitch rates were taken from `RATE.Y` and `RATE.P`, and angular acceleration was computed by centred finite differences. Fig. 17 and Table 7 report representative responses and peak values. These values describe the displayed trials rather than across-trial statistics, with signs following the corresponding body-axis convention.

6.4.3. Yaw tracking

Yaw tracking was evaluated in a single 15 m zigzag-navigation trial. A continuous 60 s segment from the middle of the flight-controller log was selected for analysis and display in Fig. 18(a). Delay was defined as the interval between a step change in commanded yaw and the onset of the actual yaw response. Overshoot was defined as the maximum excursion of the actual yaw beyond the new steady commanded value, and steady state was defined as remaining within ±5° of that value. Across the heading changes in the analysed segment, the event-level delay averaged 0.2 s (maximum: 0.7 s), and the overshoot averaged 3° (maximum: 7°).

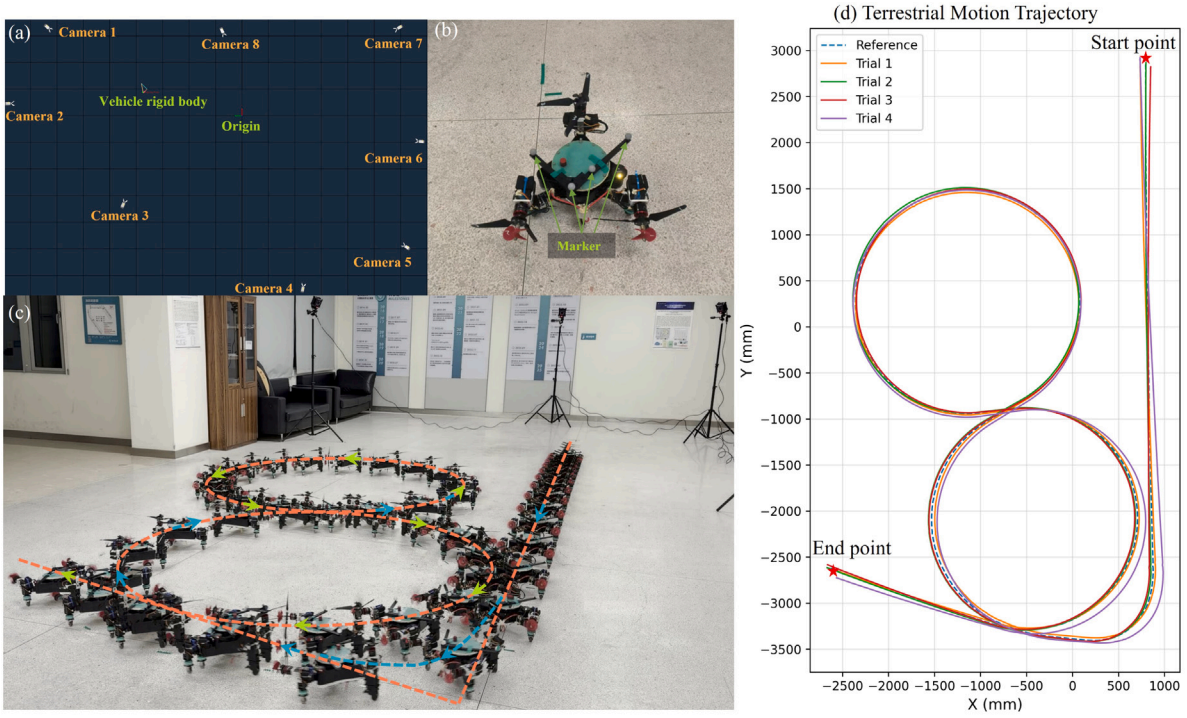


Fig. 14. Terrestrial locomotion and path-tracking performance of YingLong-T: (a) motion capture setup, (b) marker placement, (c) locomotion sequence, and (d) reference path and measured trajectories from four independent trials.

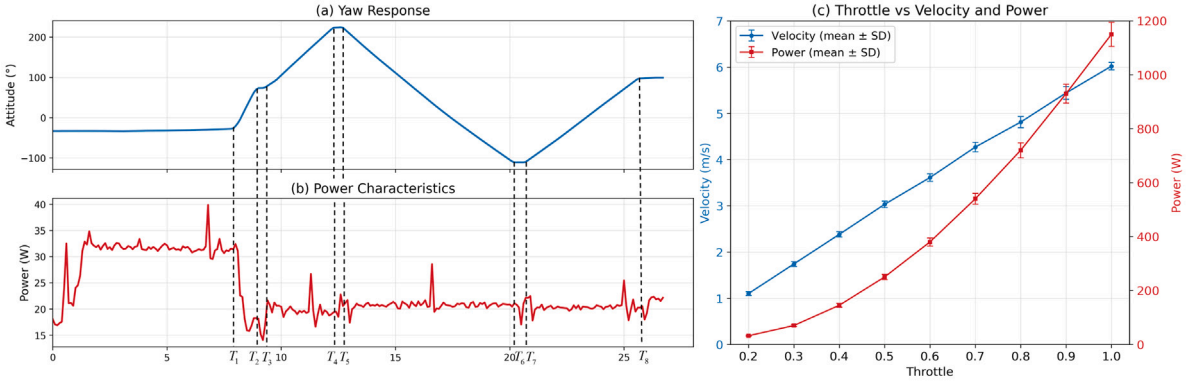


Fig. 15. Recorded terrestrial data: (a) yaw response and (b) power consumption during the representative trajectory-tracking trial, with the trajectory segments annotated; and (c) mean speed and power as functions of throttle. Error bars in (c) denote one sample standard deviation across three independent runs.

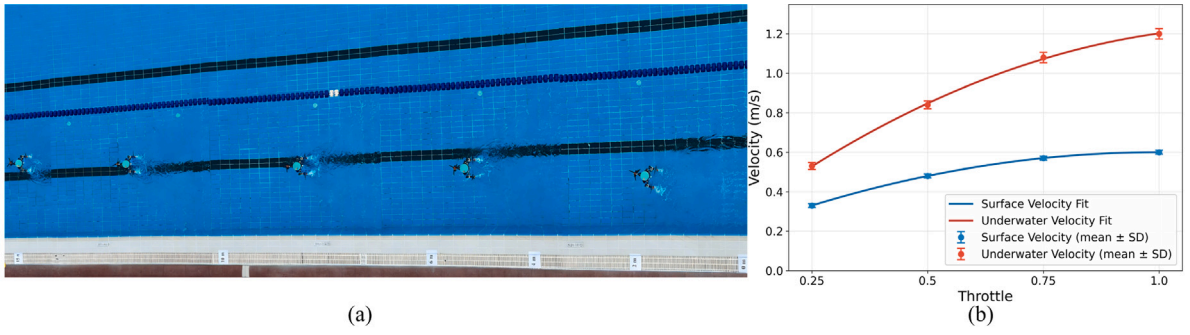


Fig. 16. WATER-domain velocity test results of YingLong-T: (a) image sequence illustrating the speed-measurement procedure and (b) mean surface and submerged speeds at different throttle levels. Error bars denote one sample standard deviation across three independent runs, and fitted curves show the overall speed–throttle trends.

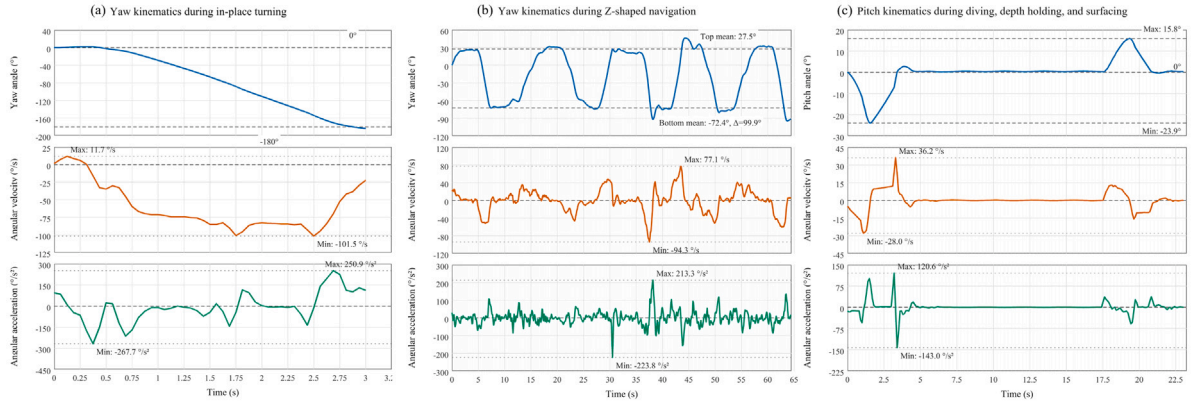


Fig. 17. Representative angular responses during (a) an in-place 180° rotation, (b) right-angle turns in Z-shaped navigation, and (c) diving–depth-keeping–surfacing. Each group shows the attitude angle, angular velocity, and angular acceleration.

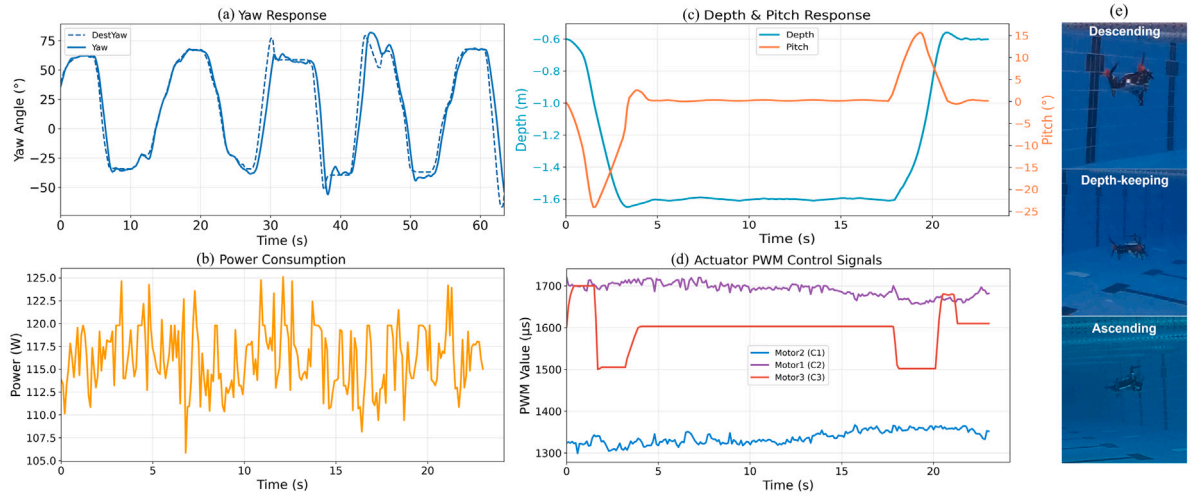


Fig. 18. Underwater yaw-tracking and depth-holding results: (a) commanded and actual yaw during the selected 60 s segment of the zigzag-navigation trial; and (b)–(e) power consumption, depth and pitch responses, actuator PWM commands, and snapshots from the displayed depth-holding trial.

6.4.4. Depth holding

Depth holding was evaluated in three independent trials using the same controller settings. Each trial used a target depth of −1.6 m and a holding duration of 15 s. Depth was measured using an MS5837 pressure sensor with a resolution of 2 mm; the water temperature during testing ranged from 20 to 30 °C.

With the aft vertical propulsion unit (M3) at neutral command (PWM ≈ 1500), the vehicle exhibits a nose-up pitch, consistent with its longitudinal mass–buoyancy offset. Increasing the M3 command to PWM ≈ 1600 brings pitch near 0°; larger commands produce negative pitch during descent. In the depth-holding trials, the controller adjusts M3's vertical thrust using pressure-derived depth feedback. The associated pitch change, within approximately ±30° in the displayed trial, is a coupled response to off-centre thrust and mass–buoyancy moments, not an independently commanded pitch angle. Among the three trials, the trial with the median steady-state depth error during the holding phase was selected for display in Fig. 18(b)–(e). In the displayed trial, the depth overshoot was approximately 6 cm, the steady-state error remained within ±2 cm, and the mean power consumption during depth holding was 115 W. With a 6S 5000 mAh battery and 10% capacity reserved for safe surfacing, the corresponding capacity-based endurance estimate was approximately 52 min.

6.5. Cross-domain transition experiments

Test environments and evidence selection. Seven complete cross-domain cycles were conducted: one in an outdoor swimming pool, three in a low-disturbance river, and three at a coastal marine aquaculture site. The pool and river trials provided the initial feasibility evidence, whereas the three coastal trials were used to calculate the quantitative transition metrics reported below and to generate the synchronized time histories. The coastal test location and local water-surface conditions are shown in Fig. 20. During the coastal trials, the local weather forecast reported a southeasterly Force 3 wind. Photographs show surface ripples; wind speed, wave height, and wave period were not measured at the site. All seven cycles were conducted with a 0.85 kg payload on the payload hanger and a fully charged battery. In all water-based experiments with the 0.85 kg payload (approximately 8.3 N of additional weight), passive buoyancy blocks were secured near the propulsion-unit servos to partially offset the payload weight and maintain positive buoyancy. The buoyancy material had a density of 80 kg/m^3 and a mass of 32 g. When fully submerged, the blocks provided approximately 3.6 N of net buoyancy in freshwater and 3.7 N in seawater.

Each cycle comprised LAND–AIR, AIR–WATER, WATER-domain submergence and surfacing, WATER–AIR, and subsequent landing. AIR–LAND was not treated as a separately timed transition because landing terminated the cycle, although safe landing was required for

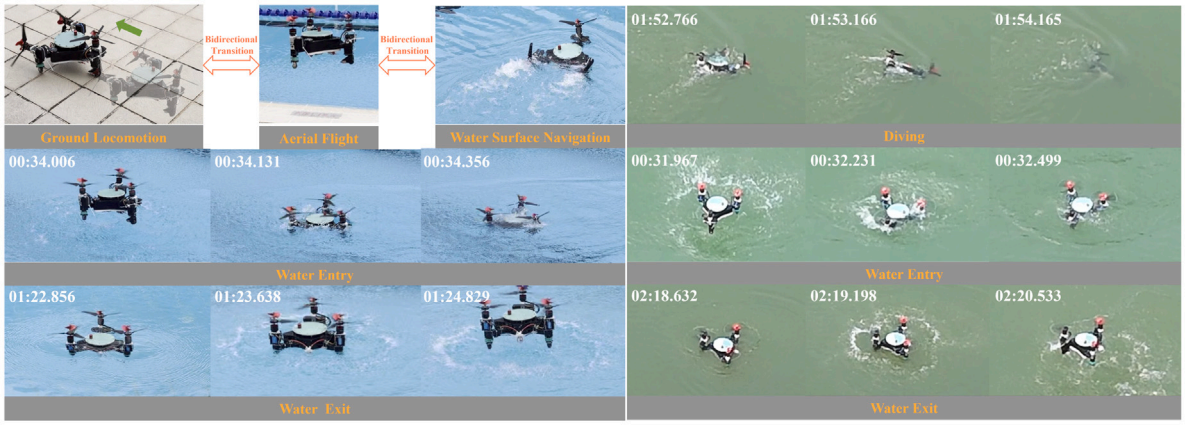


Fig. 19. Representative cross-domain experiments: (a) pool trial showing terrestrial locomotion, aerial flight, water entry, water-surface motion, and water exit; and (b) river trial showing diving, water entry, and water exit.

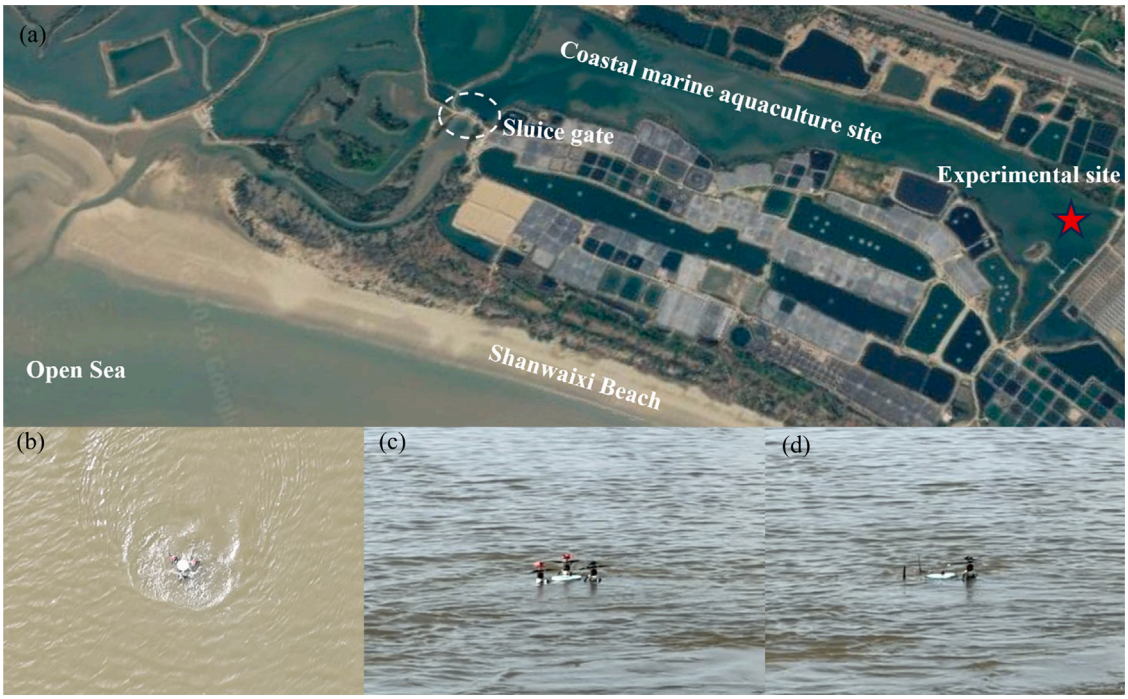


Fig. 20. Coastal marine aquaculture test site and water-surface conditions: (a) location of the test site relative to the shoreline and open sea; (b) water entry; (c) the vehicle floating after water entry; and (d) the vehicle at the surface after propulsion-unit reorientation.

successful completion. Representative pool and river sequences are shown in Fig. 19. The supplementary video presents the coastal trial with the clearest and most complete camera view; this trial was selected on the basis of recording quality rather than transition performance.

Transition definitions and timing results. The controller-level domain-switch completion criterion $S_{X\to Y} = 1$ is defined in Section 5.3. An end-to-end operational transition was considered successful when this criterion was satisfied, the corresponding physical completion criterion in Table 8 was met, and no abort or failsafe occurred. For the timing analysis, each transition was divided into three intervals:

$$\begin{aligned} t_{\mathrm{req}} &= T_{\mathrm{req}} - T_{\mathrm{stop}}, \\ t_{\mathrm{sw}} &= T_{\mathrm{commit}} - T_{\mathrm{req}}, \\ t_{\mathrm{exe}} &= T_{\mathrm{done}} - T_{\mathrm{commit}}, \\ t_{\mathrm{total}} &= t_{\mathrm{req}} + t_{\mathrm{sw}} + t_{\mathrm{exe}}, \end{aligned} \tag{22}$$

where t_{req} is the interval between termination of the source-domain motion and issuance of the switching request, t_{sw} is the controller-level domain-switching phase (DS), and t_{exe} is the transition-execution phase (TE) from domain commitment to establishment of the specified target-domain motion. Any arming delay following domain commitment is included in t_{exe}. For WATER–AIR, the vehicle had already completed surfacing and stopped underwater propulsion before the request; therefore, the measured end-to-end duration begins directly at the switching request and does not include a separate t_{req}.

The event markers used in the representative time histories are defined in Table 8. Controller requests and domain-commitment events were obtained from the flight-controller logs recorded at 10 Hz, whereas physical completion events were identified jointly from the logs and synchronized video recorded at 30 fps.

The timing statistics were calculated separately for each of the three coastal trials before computing the mean, sample standard deviation, and range. Table 9 therefore characterizes the coastal experiments only;

Table 8
Event markers for the evaluated cross-domain cycle, including WATER-domain submergence and surfacing.

Marker	Event	Experimental criterion
T_1	LAND motion completed	The commands to the two front propulsion units return to zero.
T_2	LAND–AIR request	The LAND–AIR domain-switch request is issued.
T_3	AIR domain committed	The controller-level switch is complete, with $S_{L\to A} = 1$.
T_4	LAND–AIR completed	The lowest point of the vehicle leaves the ground.
T_5	AIR motion completed	The commands to the three propulsion units return to zero.
T_6	AIR–WATER request	The AIR–WATER domain-switch request is issued.
T_7	WATER domain committed	The controller-level switch is complete, with $S_{A\to W} = 1$.
T_8	AIR–WATER completed	The front propulsion units switch to forward thrust, and WATER-domain motion begins.
T_9	Submergence initiated	Rearward propulsion is commanded to initiate submergence from the surfaced configuration.
T_{10}	Passive ascent initiated	All propulsion-motor commands return to zero, allowing passive buoyancy-driven ascent.
T_{11}	Surfacing completed	The measured depth stabilizes within $d_{eq} \pm \Delta d_{surf}$ (Table 5), and the vehicle reaches its stable surfaced configuration.
T_{12}	WATER–AIR request	The WATER–AIR domain-switch request is issued after the vehicle has reached its stable surfaced configuration.
T_{13}	AIR domain committed	The controller-level switch is complete, with $S_{W\to A} = 1$.
T_{14}	WATER–AIR completed	The lowest point of the vehicle clears the local water surface.

Table 9
Transition times measured over the three coastal-aquaculture cycles. Values are reported as mean ± sample standard deviation in seconds, with the minimum–maximum range in brackets.

Process	t_{req} (s)	t_{sw} (s) (DS)	t_{exe} (s) (TE)	t_{total} (s)	Success
LAND → AIR	1.3 ± 0.3	1.5 ± 0.1	7.3 ± 0.2	10.1 ± 0.5 [9.6–10.7]	3/3
AIR → WATER	2.7 ± 0.1	0.8 ± 0.1	1.9 ± 0.1	5.4 ± 0.1 [5.3–5.6]	3/3
WATER → AIR	–	1.1 ± 0.1	6.9 ± 0.2	8.0 ± 0.3 [7.6–8.3]	3/3

the earlier pool and river trials are not included in these numerical results.

All three coastal trials completed the prescribed sequence without an abort or failsafe. Because the experiments were manually controlled, t_{req} and t_{exe} include operator-dependent delays; consequently, t_{total} characterizes the implemented operational workflow.

Representative coastal time histories. Fig. 21 presents synchronized time histories from the representative coastal cycle. The upper colour bands indicate operation in LAND, AIR, and WATER and the intervening operational transitions: T_1–T_4 for LAND–AIR, T_5–T_8 for AIR–WATER, and T_{12}–T_{14} for WATER–AIR. Within these transition intervals, the vertical event markers identify the start and end of domain switching (DS) and subsequent transition execution (TE), as defined in Table 8. The remaining panels show actual and desired attitude, vehicle-level current and electrical power, commanded servo angles, motor PWM commands, and pressure-derived depth. Because the tilt servos have no position feedback, the plotted servo angles are commanded rather than measured values. Motor speed and individual motor current are not available from the installed ESCs; therefore, motor PWM commands and vehicle-level electrical measurements are reported instead.

The interval T_9–T_{11} is not classified as a cross-domain transition because it occurs entirely within the WATER domain. At T_9, commanded rearward propulsion initiates submergence from the surfaced configuration. The surface-submergence criterion is reached during T_9–T_{10} when the measured depth first reaches or falls below d_{imm} (Table 5). The vehicle subsequently reaches its deepest recorded position ($d = -1.02$ m); this depth was an observed value rather than a prescribed limit or success criterion.

At T_{10}, all propulsion motors are stopped, after which positive net buoyancy drives the passive ascent during T_{10}–T_{11}. During this ascent, the measured depth increases past d_{imm}. Surfacing is considered complete at T_{11}, when the depth stabilizes within $d_{eq} \pm \Delta d_{surf}$ (Table 5) and the vehicle reaches its stable surfaced configuration. In this configuration, propeller 3 is fully clear of the water, whereas propellers 1 and 2 can remain in contact with the water because the vehicle is still in the WATER configuration. The relatively large attitude variation observed during T_{10}–T_{11} indicates that the present unpowered buoyancy-driven ascent does not actively regulate attitude and remains a limitation of the current prototype.

Because the water-surface-motion interval between T_{11} and T_{12} was substantially longer than the transition intervals, a portion of this interval was omitted from both the plotted time histories and the supplementary video to present the complete cross-domain sequence more concisely. No domain-switch request, domain-commitment event, or transition-completion boundary occurred within the omitted portion;

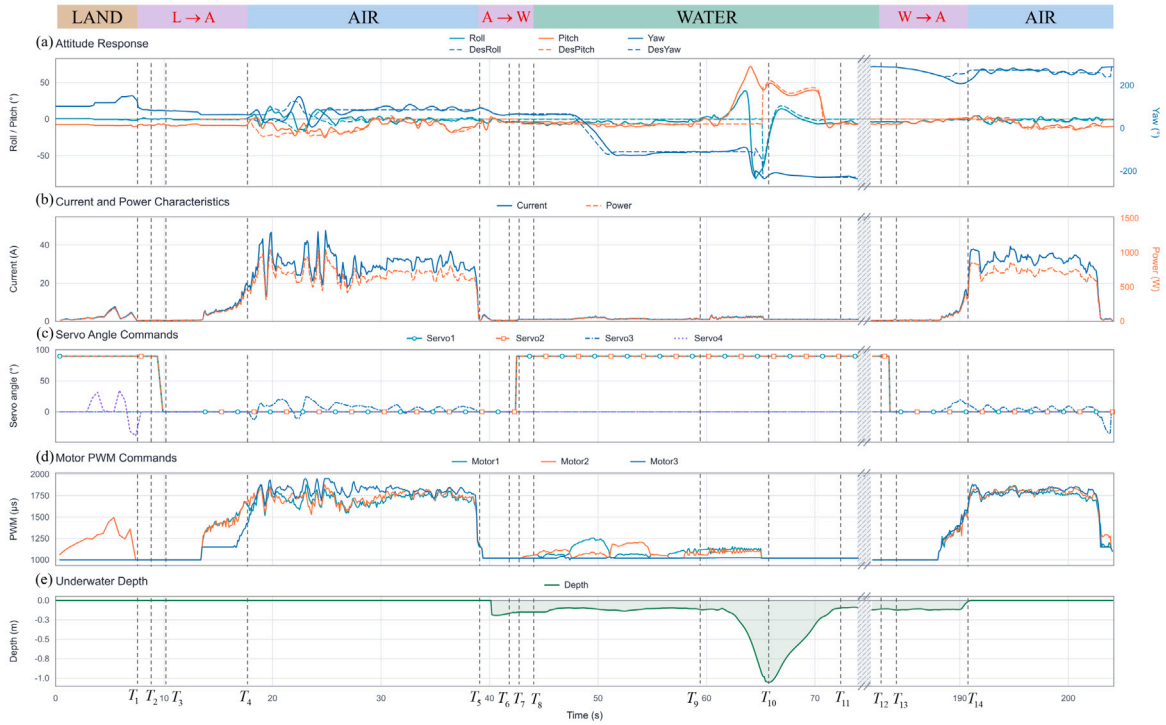


Fig. 21. Synchronized records from the representative coastal-aquaculture cycle: (a) actual and desired attitude; (b) vehicle-level current and power; (c) commanded servo angles; (d) motor PWM commands; and (e) pressure-derived depth. The upper colour bands indicate operation in each mobility domain and the intervening operational transitions; the vertical event markers T_1–T_{14} are defined in Table 8. The hatched break omits an event-free portion of sustained surface motion.

its removal therefore does not affect the reported sequence or timing definitions.

6.6. Discussion and limitations

YingLong-T reuses three propulsion units across AIR, LAND, and WATER, avoiding separate wheel-drive and underwater-thruster sets. In exchange, the system requires tilting, clutch, steering, and braking mechanisms. Sharing propulsion hardware also couples failures across domains, and the tri-rotor configuration provides no propulsion-unit redundancy in flight. This architecture prioritizes compact integration for aerial flight, short-range travel on prepared surfaces, and forward-dominant underwater inspection. Comparisons with alternative architectures remain qualitative except where quantitative results are explicitly reported.

The propeller tests support the single-clutch, same-side layout, which avoids a second clutch and an opposite-side transmission path. Compared with the aerial propeller using the same integrated hub, adding the directly driven underwater propeller caused little change in aerial thrust and reduced the thrust-to-input-power ratio by no more than $0.5\,\mathrm{gf/W}$ over the tested range. The integrated assembly also improved forward underwater performance at the tested operating points, whereas reverse operation with the clutch engaged produced limited thrust. The design accepts this small measured aerial penalty and reduced reverse propulsion authority in exchange for structural simplification.

The demonstrated mobility remains subject to configuration-specific constraints. In the LAND configuration, the small passive wheels and limited ground clearance restrict the intended operating scope to dry, flat prepared surfaces. The energy efficiency of propeller-driven rolling was not compared with powered-wheel propulsion. Underwater, the implemented allocation provides forward, depth, and yaw command channels, with roll and pitch relying on passive stability. The aft-mounted payload introduced a rearward centre-of-mass offset that may have contributed to transient pitch after takeoff and water exit; this contribution and sensitivity to payload placement were not quantified.

All cross-domain cycles were manually controlled with the same 0.85 kg payload; the timing statistics were obtained from three coastal cycles at one site. Wind speed, wave height, and wave period were not measured in situ, so their effects on transition timings cannot be isolated. These trials demonstrate sequence feasibility under the reported conditions, but do not establish statistical reliability, performance under measured sea states 1 or 2, or an open-sea operating envelope. Propeller clearance was verified only for the tested payload and surfaced configuration. Aerial propulsion remained disabled during passive emergence and reconfiguration and was enabled only after stable surfacing, satisfaction of the AIR-entry guards, and commitment of the AIR domain. The sub-GHz ELRS command and MAVLink telemetry links were used for prototype development and remained functional at the maximum tested depth of 2.5 m under one freshwater condition. This result does not establish their general operating depth, communication range, reliability, or seawater performance.

The AIR-WATER transition analysis remains qualitative, omitting configuration-dependent inertia, servo reaction moments, and time-varying free-surface hydrodynamics. These relations were not used in the implemented control laws. Long-duration freshwater and seawater tests are also needed to establish the durability of the tilt mechanisms, clutch, bearings, seals, and propulsion components.

7. Conclusions and future work

This paper presented YingLong-T, a compact vehicle that integrates a triangular body, a unified reconfigurable powertrain, and a multi-domain control architecture implemented on a single flight controller. The integrated body serves as the load-bearing airframe, houses the on-board electronics in a watertight enclosure, and provides the vehicle's primary buoyancy. The three shared propulsion units support tri-rotor flight, propeller-driven ground rolling, and Y3 underwater propulsion.

Positive buoyancy and propulsion-unit reorientation enable staged air–water transitions without active buoyancy adjustment. The principal contribution lies in the coordinated design and system-level integration of these functions, building on established locomotion, propulsion, and control principles.

The 2.5 kg prototype was evaluated with an 850 g payload in all three mobility domains and during cross-domain transitions. The tests demonstrated manual flight, a maximum ground speed of 6.1 m/s, and a mean terrestrial tracking RMSE of 45.6 ± 23.6 mm. Underwater tests recorded a maximum mean submerged speed of 1.20 m/s, while the representative depth-holding trial showed steady-state depth error within ±2 cm. All seven evaluated cross-domain cycles were completed under the reported conditions. Across the three coastal trials, the mean domain-switching durations ranged from 0.8 to 1.5 s, and the mean end-to-end transition durations ranged from 5.4 to 10.1 s.

These results demonstrate prototype feasibility under the tested conditions. The transitions were manually controlled, and the tests did not systematically vary payload or field conditions, measure environmental disturbances in situ, or assess long-term durability.

Future work will improve vehicle balance by redistributing the battery, electronics, and payload or introducing an adjustable payload mount, and extend ground mobility through larger wheels, improved wheel grip, and increased propulsion-unit clearance. Control development will focus on autonomous transitions and a YingLong-T-specific vector-thrust allocator with tilt-position feedback to extend underwater control authority, together with the development and validation of a coupled transition model. These improvements will be evaluated through controlled tests under varied payloads, initial states, terrain, waves, and currents to establish operating limits, followed by extended freshwater and seawater endurance trials before operational marine deployment.

CRediT authorship contribution statement

Le Huang: Writing – original draft, Methodology, Formal analysis, Conceptualization. **Shuxiang Guo:** Supervision, Project administration, Funding acquisition. **Qirong Lei:** Writing – review & editing, Data curation. **Miaozhang Shen:** Validation, Formal analysis. **Chunying Li:** Supervision. **Siying Pu:** Validation, Investigation. **Shuaixin Peng:** Investigation, Data curation. **Guoheng Ma:** Investigation, Data curation. **Jinglei Nie:** Investigation, Data curation. **Pengcheng Li:** Investigation, Data curation.

Declaration of competing interest

The authors declare that they have no known competing financial interests or personal relationships that could have appeared to influence the work reported in this paper.

Acknowledgements

This work was supported in part by the Guangdong Basic and Applied Basic Research Foundation General Program under Grant 2025A1515011007, in part by the Shenzhen Science and Technology Program under Grant RCBS20231211090725048, in part by the High Level of Special Funds from Southern University of Science and Technology under Grant G03034K003, in part by the Guangdong Provincial Science and Technology Innovation Strategy Special Fund (Climbing Plan) under Grant pdjh2025bc188, and in part by the Guangdong College Students' Scientific and Technological Innovation Cultivation Fund (Climbing Program) under Grant pdjh2026c11009.

Appendix A. Supplementary data

Supplementary material related to this article can be found online at https://doi.org/10.1016/j.oceaneng.2026.129153.

References

Alzu'bi, H., Akinsanya, O., Kaja, N., Mansour, I., Rawashdeh, O., 2015. Evaluation of an aerial quadcopter power-plant for underwater operation. In: 2015 10th International Symposium on Mechatronics and Its Applications. ISMA, pp. 1–4. http://dx.doi.org/10.1109/ISMA.2015.7373488.

ArduPilot Development Team, 2026. ArduSub SimpleROV-3 motor allocation in AP_Motors6DOF.cpp. Source code, https://github.com/ArduPilot/ardupilot/blob/master/libraries/AP_Motors/AP_Motors6DOF.cpp. (Accessed 26 September 2026).

Bai, Y., Jin, Y., Liu, C., Zeng, Z., Lian, L., 2023. Nezha-F: Design and analysis of a foldable and self-deployable HAUV. IEEE Robotics Autom. Lett. 8 (4), 2309–2316.

Baines, R., Patiballa, S.K., Booth, J., Ramirez, L., Sipple, T., Garcia, A., Fish, F., Kramer-Bottiglio, R., 2022. Multi-environment robotic transitions through adaptive morphogenesis. Nature 610 (7931), 283–289.

Bambu Lab, n.d.-a., PA6-CF technical data sheet. URL: https://store.bblcdn.eu/s8/default/a64af9edb0f64095ad18bc4ad4faf1ec/Bambu_PA6-CF_Technical_Data_Sheet-v2.pdf. (Accessed 2 October 2026).

Bambu Lab, n.d.-b, PC technical data sheet. p. 2, URL: https://store.bblcdn.eu/s8/default/ab03007d58814bc28a08145719b552de/Bambu_PC_Technical_Data_Sheet.pdf, Version 3.0, (Accessed 2 October 2026).

Bambu Lab, n.d.-c., PA6-GF technical data sheet. p. 2, URL: https://store.bblcdn.eu/s8/default/ed63c87506bf4520a276419f7dad919c/Bambu_PA6-GF_Technical_Data_Sheet.pdf, Version 1.0, (Accessed 2 October 2026).

Bi, Y., Xu, Z., Shen, Y., Zeng, Z., Lian, L., 2024. Design and implementation of a bone-shaped hybrid aerial underwater vehicle. IEEE Robotics Autom. Lett. 9 (8), 7318–7325. http://dx.doi.org/10.1109/LRA.2024.3420550.

Canelon, D., Westlake, S., Wang, Y., Papanikolopoulos, N., 2021. Design and characterization of a multi-domain unmanned vehicle operating in aerial, terrestrial, and underwater environments. In: 2021 International Conference on Unmanned Aircraft Systems. ICUAS, pp. 1466–1471.

Cao, M., Xu, X., Yuan, S., Cao, K., Liu, K., Xie, L., 2023. DoubleBee: A hybrid aerial-ground robot with two active wheels. In: 2023 IEEE/RSJ International Conference on Intelligent Robots and Systems. IROS, pp. 6962–6969.

Chaikalis, D., Evangeliou, N., Nabeel, M., Giakoumidis, N., Tzes, A., 2023. Mechatronic design and control of a hybrid ground-air-water autonomous vehicle. In: 2023 International Conference on Unmanned Aircraft Systems. ICUAS, pp. 1337–1342.

Evangeliou, N., Chaikalis, D., Giakoumidis, N., Tzes, A., 2023. Mechatronic design of an amphibious drone. In: 2023 9th International Conference on Automation, Robotics and Applications. ICARA, pp. 230–233.

Gao, Y., Zhang, H., Li, G.J., Zhou, M., Yin, H., Gulliver, T.A., 2023. Analysis of trans-domain motion process of bullet-shaped trans-domain amphibious vehicle. J. Field Robotics 41, 68–92.

Gómez-Ortega, A., Piedra, S., Mondragón-Rodríguez, G.C., Camacho, N., 2024. Dependence of the mechanical properties of nylon-carbon fiber composite on the FDM printing parameters. Compos. Part A: Appl. Sci. Manuf. 186, 108419. http://dx.doi.org/10.1016/j.compositesa.2024.108419.

Gonzalez, Y.E., Mendoza, J.M., Restrepo Durán, J., Tapia Vertel, L.C., Rhenals-Julio, J.D., 2023. Effect of printing parameters on mechanical properties and processing time of additively manufactured parts. Matéria (Rio de Janeiro) 28 (3), e20230111. http://dx.doi.org/10.1590/1517-7076-RMAT-2023-0111.

Guo, J., Zhang, K., Guo, S., Li, C., Yang, X., 2019. Design of a new type of tri-habitat robot. In: 2019 IEEE International Conference on Mechatronics and Automation. ICMA, pp. 1508–1513.

Guo, Z., Zhu, Y., Wang, M., Li, T., Zhao, H., Xu, L., Ceccarelli, M., 2019. System design and experimental analysis of an all-environment mobile robot. Adv. Mech. Mach. Sci.

Jin, Y., Bi, Y., Lyu, C., Bai, Y., Zeng, Z., Lian, L., 2023. Nezha-IV: A hybrid aerial underwater vehicle in real ocean environments. J. Field Robotics 41, 420–442.

Jin, Y., Zeng, Z., Lian, L., 2025. Nezha-SeaDart: A tail-sitting fixed-wing vertical takeoff and landing hybrid aerial underwater vehicle. J. Field Robotics 42 (1), 137–152. http://dx.doi.org/10.1002/rob.22399.

Jin, Y., Zeng, Z., Lian, L., 2026. Nezha-SeaDart III: A VTOL tail-sitting vehicle with versatile dual-medium thrusters. Ocean Eng. 352, 124619. http://dx.doi.org/10.1016/j.oceaneng.2026.124619.

Li, X., Lai, T., Lai, M., Lin, J., Zhang, M., Zhi, J., Xu, C., Gao, F., Cao, Y., 2026. TriphiBot: A triphibious robot combining FOC-based propulsion with eccentric design. arXiv:2602.01385.

Li, L., Wang, S., Zhang, Y., Song, S., Wang, C., Tan, S., Zhao, W., Wang, G., Sun, W., Yang, F., Liu, J., Chen, B., Xu, H., Nguyen, P., Kovac, M., Wen, L., 2022. Aerial-aquatic robots capable of crossing the air-water boundary and hitchhiking on surfaces. Sci. Robotics 7 (66), eabm6695.

Liu, X., Dou, M., Huang, D., Gao, S., Yan, R., Wang, B., Cui, J., Ren, Q., Dou, L., Gao, Z., Chen, J., Chen, B.M., 2023. TJ-FlyingFish: Design and implementation of an aerial-aquatic quadrotor with tiltable propulsion units. In: 2023 IEEE International Conference on Robotics and Automation. ICRA, pp. 7324–7330.

Liu, K., Xiao, J., Peng, H., Zhang, Y., Zhao, S., Lu, H., Huang, K., 2026. Transition strategy for unmanned aerial–aquatic vehicles (UAAVs): A survey. J. Field Robotics http://dx.doi.org/10.1002/rob.70138.

Mitchell, D., Blanche, J., Harper, S., Lim, T., Gupta, R., Zaki, O., Tang, W., Robu, V., Watson, S., Flynn, D., 2022. A review: Challenges and opportunities for artificial intelligence and robotics in the offshore wind sector. Energy AI 8, 100146. http://dx.doi.org/10.1016/j.egyai.2022.100146.

Qin, K., Tang, W., Zhong, Y., Liu, Y., Xu, H., Zhu, P., Yan, D., Yang, H., Zou, J., 2023. An aerial–aquatic robot with tunable tilting motors capable of multimode motion. Adv. Intell. Syst. 5, URL: https://api.semanticscholar.org/CorpusID:261502833.

Quan, Q., 2017. Introduction to Multicopter Design and Control. Springer, Singapore, http://dx.doi.org/10.1007/978-981-10-3382-7.

Rockenbauer, F.M., Jeger, S.L., Beltrán, L., Berger, M., Harms, M., Kaufmann, N., Rauch, M., Reinders, M., Lawrance, N.R.J., Stastny, T., Siegwart, R.Y., 2021. Dipper: A dynamically transitioning aerial-aquatic unmanned vehicle. Robotics: Sci. Syst. XVII URL: https://api.semanticscholar.org/CorpusID:235650748.

Sihite, E., Kalantari, A., Nemovi, R., Ramezani, A., Gharib, M., 2023. Multi-modal mobility morphobot (M4) with appendage repurposing for locomotion plasticity enhancement. Nat. Commun. 14 (1), 3323.

Sun, X., Cao, J., Li, Y., Wang, B., 2023. Design and field test of a foldable wing unmanned aerial–underwater vehicle. J. Field Robotics 41, 347–373.

T-MOTOR, 2026. T-MOTOR multirotor motor and propeller static thrust test data. Manufacturer datasheets and online product specifications, URL: https://store.tmotor.com/, Used for motor mass, propeller mass, thrust, power, current, and efficiency data. (Accessed 08 July 2026).

Wang, J., Aoran, M., Yaojia, M., Zhongxue, G., Guoniu, Z., 2025. Research status and future prospects of biomimetic amphibious robots. Robot 47 (2), 283–304.

Wang, Z., Jiang, Y., Zou, Z., Zhen, Z., 2024. Design and implementation of a multimodal tilt-rotor unmanned aerial-aquatic vehicle. J. Field Robotics 42 (5), 1766–1782. http://dx.doi.org/10.1002/rob.22478.

Xing, H., Liu, C., Guo, S., Shi, L., Liu, W., Liu, H., Zhao, Y., 2022. Research on multi-mode motion of the miniature amphibious turtle-inspired robot. Robot 44 (2), 212–223.

Yang, S., Xue, K., Lv, M., Xu, Y., Yang, J., Lu, Y., Liu, C., Qian, H., 2022. Design and verification of a novel triphibian robot. arXiv:2211.17022.

Yu, F., Chen, Y., 2019. Trajectory tracking control of an amphibian robot with operational capability. Int. J. Adv. Robotic Syst. 16.

Zheng, Z., Xu, Q., Feng, Y., Dai, Y., Chen, Z., Wu, Y., 2026. Optimization design of a pre-swirl duct for a container ship: A simulation-based design method integrating a support vector regression surrogate model. Ocean Eng. 352, 124574.

Zhong, G., Cao, J., Chai, X., Bai, Y., 2021. Design and performance analysis of a triphibious robot with tilting-rotor structure. IEEE Access 9, 10871–10879.